nrap

National Risk
Assessment Partnership

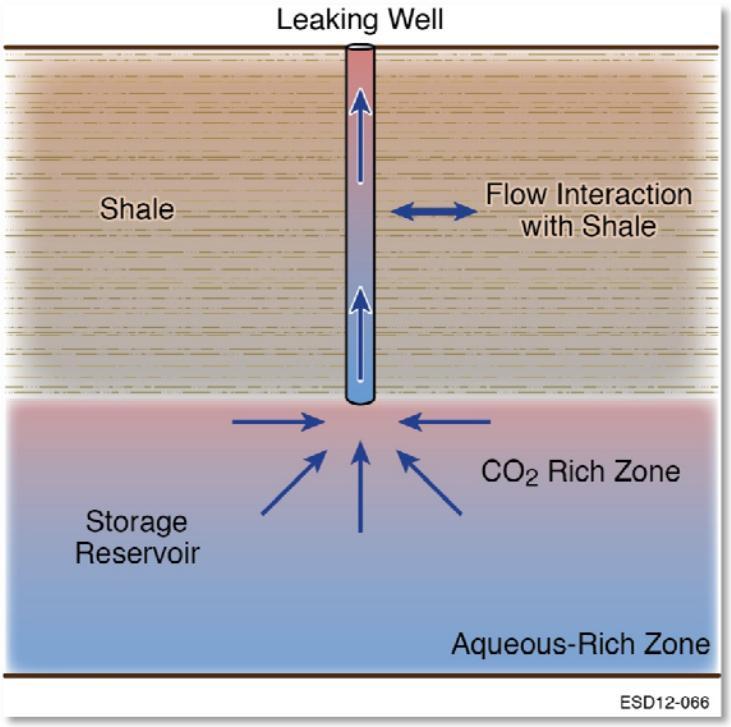

Assessment of Decoupling Wellbore Leakage from Reservoir Flow in Reduced-Order Models

3 January 2013

U.S. DEPARTMENT OF ENERGY

NETL

Office of Fossil Energy

NRAP-TRS-III-001-2013

Disclaimer

This report has been reviewed by Hui-Hai Liu and approved for public release.

Cover Illustration: Conceptual diagram of well leakage through a shale caprock from a storage reservoir containing brine and injected CO_2.

Suggested Citation: Houseworth, J.; Wainwright, H.; Birkholzer, J. *Assessment of Decoupling Wellbore Leakage from Reservoir Flow in Reduced-Order Models*; NRAP-TRS-III-001-2013; NRAP Technical Report Series; U.S. Department of Energy, National Energy Technology Laboratory: Morgantown, WV, 2013; p 60.

An electronic version of this report can be found at: www.netl.doe.gov/nrap

Assessment of Decoupling Wellbore Leakage from Reservoir Flow in Reduced-Order Models

Jim Houseworth[1], Haruko Wainwright[1], and Jens Birkholzer[1]

[1]Earth Sciences Division, Lawrence Berkeley National Laboratory, 1 Cyclotron Road Berkeley, CA 94720

NRAP-TRS-III-001-2013

Level III Technical Report Series

3 January 2013

This page intentionally left blank

Table of Contents

1. EXECUTIVE SUMMARY 1

2. INTRODUCTION 3

3. AN EXAMPLE OF WELL LEAKAGE COUPLED WITH RESERVOIR FLOW 5

4. NUMERICAL MODEL OF WELL LEAKAGE COUPLED WITH THE STORAGE RESERVOIR 8

4.1 MODELING DOMAIN AND NUMERICAL GRID 8

4.2 BOUNDARY AND INITIAL CONDITIONS 9

4.3 CASES INVESTIGATED 10

4.4 PROPERTIES USED FOR THE SIMULATIONS 11

4.5 FLOW BEHAVIOR 13

4.6 SIMULATION RESULTS FOR WELL-RESERVOIR COUPLING 26

4.7 SIMULATION RESULTS FOR WELL SATURATION 33

4.8 SIMULATION RESULTS FOR WELL TEMPERATURE 34

5. PHYSICS-BASED REDUCED-ORDER MODELS 36

5.1 UNCALIBRATED RESULTS AND CALIBRATION DIRECTLY USING FITTING COEFFICIENTS 37

5.2 CALIBRATION USING CORRELATIONS FOR SATURATION AND AQUEOUS DENSITY IN THE WELL 38

6. DISCUSSION OF ALTERNATIVE PROMS 41

7. SUMMARY AND CONCLUSIONS 43

8. REFERENCES 45

APPENDIX – PROM CALIBRATIONS TO AN UNCOUPLED WELL-LEAKAGE PROCESS MODEL 1

List of Figures

Figure 1: Domain diagram for simple coupled well leakage-reservoir model. 5

Figure 2: Model domain and boundary conditions. 8

Figure 3: Numerical grid. (a) entire domain; (b) detail near well-reservoir interface. 9

Figure 4: Initial reservoir saturations distributions: (a) average CO_2 saturation 0.01; (b) average CO_2 saturation 0.2; and (c) average CO_2 saturation 0.5. 10

Figure 5: Phases, components, and mass transport during well leakage. 15

Figure 6: Steady-state results for leakage case rg53 (k_b = 1 darcy, k_r = 0.1 darcies, S_g = 0.5, R_{op} = 1.3 MPa). (a) H_2O mass flow rate along well; (b) CO_2 phase saturation along well; (c) radial pressure profile along top of reservoir. 16

Figure 7: CO_2 saturation contours for case rg53 (k_b = 1 darcy, k_r = 0.1 darcies, S_g = 0.5, R_{op} = 1.3 MPa). 17

Figure 8: Primary transient well leakage at ground surface for rg53 (k_b = 1 darcy, k_r = 0.1 darcies, S_g = 0.5, R_{op} = 1.3 MPa). 17

Figure 9: Primary transient well leakage at surface for thick-layer cases. Tables 2 and 3 present complete definitions of the different cases. 18

Figure 10: Results for leakage case rg46 (k_b = 1,000 darcy, k_r = 0.01 darcies, S_g = 0.2, R_{op} = 0.99 MPa).. 20

Figure 11: Results for leakage case rg22 (k_b = 1 darcy, k_r = 0.01 darcies, S_g = 0.01, R_{op} = 0.74 MPa). 22

Figure 12: Results for leakage case rg31 (k_b = 1,000 darcy, k_r = 0.01 darcies, S_g = 0.01, R_{op} = 0.74 MPa).. 24

Figure 13: Average aqueous density in well versus dimensionless parameter, F_c. 25

Figure 14: Water saturation profile for two cases of leaking wells that are the same except for the shale permeability (k_s). 26

Figure 15: Ratio between well CO_2 flow rates for shale permeability of 10^{-7} darcy to that for shale permeability of 10^{-18} darcy, R_{op} = 1.2 MPa and average CO_2 saturation of 0.53 for both cases. 26

Figure 16: CO_2 and H_2O flow rates and CO_2 saturations and pressures at the base of the well for different combinations of reservoir and well permeabilities 28

Figure 17: CO_2 and H_2O flow rates and CO_2 saturations and pressures at the base of the well for different combinations of reservoir and well permeabilities 29

Figure 18: CO_2 and H_2O flow rates and CO_2 saturations and pressures at the base of the well for different combinations of reservoir and well permeabilities 30

Figure 19: CO_2 and H_2O flow rates and CO_2 saturations and pressures at the base of the well for different combinations of reservoir and well permeabilities 31

Figure 20: CO_2 and H_2O flow rates and CO_2 saturations and pressures at the base of the well for different combinations of reservoir and well permeabilities 33

Figure 21: Unperturbed CO_2 saturations in the reservoir at the base of the well versus average CO_2 saturation in the supercritical region in the well. 34

Figure 22: Temperature profiles in well.. 35
Figure 23: Uncalibrated PROMs that use unperturbed reservoir saturations for the well.. 38
Figure 24: Calibrated PROMs that use unperturbed reservoir saturations for the well. 38
Figure 25: Correlation between Average Water Saturation in Supercritical Region of Well with Well Permeability, Reservoir Overpressure, and Reservoir Permeability. 39
Figure 26: PROMs that use a saturation correlation function and aqueous density correlation function..... 40
Figure 27: Multi-phase, multi-component PROMs using a numerical simulation approach..... 41
Figure 28: Analytical PROMs. 42

List of Tables

Table 1: Cases investigated..... 11
Table 2: Permeability combinations 11
Table 3: Simulation properties..... 12

This page intentionally left blank

Acronyms and Abbreviations

Term	Description
DOE	Department of Energy
ECO2M	LBNL module for equations of state for CO_2
LANL	Los Alamos National Laboratory
LBNL	Lawrence Berkeley National Laboratory
NETL	National Energy Technology Laboratory
NRAP	National Risk Assessment Partnership
PROM	Physics-based reduced-order model
RMSE	Root-mean-square relative error
TOUGH2	Transport of Unsaturated Groundwater and Heat (LBNL reservoir simulator)

Symbols

Symbol	Definition and Units
Q_r	Mass flow rate in the reservoir (kg/s)
k_r	Reservoir permeability (m^2, darcy)
$p(r)$	Gas pressure (Pa) as a function of radial distance from well inlet
ρ_g	Gas density (kg/m^3)
g	Gravitational acceleration (9.8066 m/s^2)
k_b	Wellbore permeability (m^2, darcy)
Q_b	Mass flow rate in the wellbore (kg/s)
r_b	Well radius (m)
L	Well length (m)
p_{atm}	Atmospheric pressure (Pa)
ρ_w	Water density (kg/m^3)
r_{hs}	Radial distance to hydrostatic boundary (m)
R_{op}	Reservoir overpressure (Pa, MPa)
z	Vertical coordinate (m)
r	Radial coordinate (m)
ν_g	Gas kinematic viscosity (m^2/s)
Δp	Variation in pressure (from hydrostatic plus overpressure) caused by well leakage at the base of the well (Pa)
$\overline{\rho_g}$	Gas density averaged over the well depth (kg/m^3)
$\overline{\nu_g}$	Gas kinematic viscosity averaged over the well depth (kg/m^3)
S_g	Average gas saturation in reservoir (unitless)
T	CO_2 layer thickness at the top of the reservoir (m)
p_c	Capillary pressure (Pa)
α	van Genuchten capillary strength (Pa^{-1})

m	van Genuchten pore-size distribution parameter (unitless)
S_w	Water saturation (unitless)
S_{wn}	Normalized water saturation for water relative permeability (unitless)
S_{wr}	Residual water saturation (unitless)
k_{rw}	Relative permeability to water (unitless)
k_{rg}	Relative permeability to gas (unitless)
S_{gr}	Residual gas saturation (unitless)
$\hat{S}_{wn}$	Normalized water saturation for gas relative permeability (unitless)
F_c	Dimensionless group for reservoir flow behavior (unitless)
$\dot{m}_g$	Mass flow rate of CO_2 in well (kg/s)
$\dot{m}_w$	Mass flow rate of H_2O in well (kg/s)
A	Cross-sectional area of well (m^2)
ν_w	Water kinematic viscosity (m^2/s)
β_g	Calibration parameter for CO_2 mass flow rate in well (unitless)
β_w	Calibration parameter for H_2O mass flow rate in well (unitless)
X	Mass fraction of H_2O in CO_2 (unitless)
S_{gb}	Average CO_2 saturation within supercritical region in the well (unitless)
β	Calibration parameter for uncoupled PROMs for CO_2 and H_2O well leakage (unitless)
a_j , j=0 to 15	Regression parameters for CO_2 saturation correlation (unitless)
S_{CO_2}	CO_2 saturation at bottom of well (unitless)
$\left(\frac{P_b - P_s}{D}\right)_n$	Normalized average pressure gradient (unitless)
P_b	Fluid pressure at base of well (Pa)
P_s	Fluid pressure at top of well (Pa)
c_{gj} , j = 0 to 5	Correlation parameters for uncoupled gas leakage rate model (unitless)
T_b	Temperature at base of well (°C)
c_{wj} , j = 0 to 11	Correlation parameters for uncoupled water leakage rate model (unitless)

Acknowledgments

This work was completed as part of National Risk Assessment Partnership (NRAP) project. Support for this project came from the Department of Energy's (DOE) Office of Fossil Energy Crosscutting Research program. The authors wish to acknowledge Robert Romanosky (National Energy Technology Laboratory [NETL] Strategic Center for Coal) and Regis Conrad (DOE Office of Fossil Energy) for programmatic guidance, direction, and support.

NRAP funding was provided to Lawrence Berkeley National Laboratory (LBNL) under U.S. DOE Contract No. DE-AC02-05CH11231.

The authors also thank Amy Jordan and Phil Stauffer of Los Alamos National Laboratory (LANL) for providing the uncoupled well-leakage process model results presented in the Appendix along with helpful discussions concerning their results, and H. H. Liu and Daniel Hawkes for constructive reviews of this report

1. EXECUTIVE SUMMARY

The potential leakage of CO_2 and brine through wells is a process that requires investigation to assess risk associated with geologic CO_2 sequestration. The National Risk Assessment Partnership (NRAP) is developing system-level simulators to represent major system components used to quantify risk. These risk assessments are computationally intensive for a number of reasons, in part because stochastic simulation methods are needed for uncertainty quantification and in part because of the complexity of geologic systems involved in CO_2 sequestration. Therefore, there is a need to reduce the computational burden associated with detailed process-level models for system-level risk assessments. This is done through the use of reduced-order models, which are used as surrogates for the more precise process-level models in system-level simulations but are more efficient computationally. One of the simplifications employed for reduced-order models of CO_2 leakage through wells is that the CO_2 leakage process may be decoupled from flow processes that occur in the reservoir induced by well leakage. This report summarizes analyses performed for a storage reservoir coupled with a leaking well to assess the suitability of the decoupling approximation. Other simplifications used by reduced-order models include quasi-steady-state leakage and minimal interactions between leakage flow and the caprock. The analyses performed for decoupling also provide information relative to these simplifications.

Coupled well leakage with reservoir flow effects were investigated using a process-level model to investigate well leakage over a range of initial conditions and permeability levels in the leaking well and reservoir. Coupled effects between the reservoir flow restrictions and well leakage have been found to be relatively weak if well-to-reservoir permeability ratios are 100 or less and if CO_2 saturations in the reservoir are not too small. For higher CO_2 saturations in the reservoir, the maximum effect of coupling on well leakage is less than a factor of three even for well-to-reservoir permeability ratios of 10^5. However, coupled effects on well leakage can be stronger when CO_2 occupies a relatively thin layer along the top of the reservoir. For thin-layer cases with large well to reservoir permeability ratios, the leakage rates can vary by nearly two orders of magnitude as a result of coupling with the reservoir.

The reservoir CO_2 saturation immediately below the well was found to change in response to well leakage. However, the saturation in the well cannot be entirely explained by either the initial reservoir saturation state or even to the saturation at the base of the well during the leakage. The saturation in the well was found to be correlated with various factors such as well permeability, reservoir overpressure, and reservoir permeability, in addition to saturation in the reservoir. These results suggest that some degree of coupling is needed in the well-leakage process model used to calibrate a well-leakage reduced-order model in order to represent the saturation differences between the reservoir and the well.

Process-model simulations also provided information on transient well leakage. Two types of transients were identified: primary transients that occur as CO_2 initially moves up the well and for cases with a thin CO_2 layer in the reservoir, secondary transients occurred as a result of coupling between well leakage and reservoir flow. Results show that the duration of the primary transient response, in which CO_2 initially moves up the well, for a one-Darcy well is about 100 years. Durations were found to be roughly proportional to the inverse of the well permeability. Secondary transients were found to have much longer durations (~100,000 years) but in most cases tended to have a weaker influence on well leakage than primary transients. However, in the

most extreme case, a secondary transient persisted for more than 250,000 years during which the CO_2 leakage rate decreased by about 98 percent from its peak value shortly after CO_2 breakthrough. Because CO_2 leakage rates always rise to a maximum steady-state value as a result of primary transients, use of a steady-state approximation for CO_2 leakage overestimates CO_2 leakage. On the other hand, secondary transients lead to a decrease in CO_2 leakage rates following the primary transient; therefore, use of the steady-state leakage rate underestimates leakage when secondary transients occur.

Calculation results suggested that the overlying shale would be important not only for the heat exchange but also for the water exchange during the leakage, especially in the long-term behavior. The presence of semipermeable shale may have two competing effects: (1) increase CO_2 saturation in a leaky well, which could increase CO_2 relative permeability and CO_2 leakage rate; and (2) more rapidly dissipate overpressure, which could reduce the leakage rate.

Physics-based reduced-order models (PROMs) were investigated employing a quasi-steady-flow approximation and Darcy's equation for two-phase flow. It was necessary to calibrate the PROMs to estimate saturation in the well through a correlation with well permeability, reservoir overpressure, reservoir permeability, and the initial CO_2 saturation below the well. Calibration for aqueous density in the well was also required because of significant dissolution/exsolution processes for H_2O in CO_2 affecting the water composition in the well. The PROMs give results with mean-square relative errors of 38 percent for CO_2 and 52 percent for H_2O mass flow rates as compared with process-level simulations.

The analytical PROMs investigated here address multi-phase, multi-component effects using correlations developed from process-level modeling to incorporate the more complex effects of phase saturation and aqueous density in the well. However, the results here do not address several aspects of system variability, including the effects of different relative permeability parameters, well penetration into the storage reservoir, and well depth. Furthermore, additional significant complexities identified in this report, in particular transient effects and interactions of well leakage with low-permeability shales still require further PROM development. More complex PROMs appear to be necessary to address these issues; otherwise, substantial conservatism may be required to avoid underestimation of leakage risk.

2. INTRODUCTION

The goal of geologic CO_2 storage is to prevent carbon dioxide, released primarily through combustion of fossil fuels, from entering the atmosphere. This is accomplished by permanently trapping CO_2 in deep geologic formations. CO_2 exists as a supercritical fluid under pressure and temperature conditions of geologic formations, which is being investigated for CO_2 storage. Prior to CO_2 injection, storage formations are commonly saturated with saline water, which is relatively immiscible with supercritical CO_2. The supercritical CO_2 is also typically less dense than the saline water, which leads to buoyancy forces that can act to drive CO_2 upwards from the storage formation into shallower formations or to the ground surface if permeable flow pathways exist between the storage reservoir and the ground surface through the overlying strata. In addition, the act of CO_2 injection into a storage reservoir can also increase the fluid pressure in the reservoir. This increased fluid pressure can also act to drive both CO_2 and brine out of the storage reservoir if permeable pathways are present.

A geologic formation must have certain characteristics in order to be considered as a potential storage formation for geologic CO_2 storage. The formation needs to be sufficiently deep such that CO_2 exists as a supercritical fluid and must have sufficient storage capacity. Other characteristics include sufficient permeability for injection of large volumes of CO_2. A significant characteristic is that the storage reservoir must be capped by an adequate sealing formation of low-permeability rock. The purpose of the sealing formation is to prevent the natural tendency for CO_2 to rise from buoyancy and injection pressure effects. One of the potential leakage pathways for CO_2 to escape from a storage reservoir is along wells (Benson and Cook, 2005). Properly installed wells that are either in use, or plugged and abandoned, do not present a preferential flow pathway for fluids to leak out of the storage reservoir. However, a number of factors can cause a loss of well integrity, such that leakage is possible (Bachu and Bennion, 2009; Carey et al., 2007; Carey et al., 2010; Duguid et al., 2011).

An assessment of geologic CO_2 storage requires consideration of potential leakage of CO_2 and brine through wells that may present preferential pathways (Benson and Cook, 2005). This assessment involves a complex geologic system that includes flow of CO_2 and saline water within the storage reservoir in response to CO_2 injection interacting with leakage pathways such as wells (Nordbotten et al., 2009; Ebigbo, et al., 2007). The approach being used by the National Risk Assessment Partnership (NRAP) is to quantify risks of geologic CO_2 storage using system-level models for the major system components of the storage reservoir, potable aquifer, and leakage pathways such as wells. These models require efficient computational methods to enable large numbers of stochastic simulations for uncertainty quantification, leading to use of reduced-order models as surrogates for more precise but less efficient process-level models (Razavi et al., 2012).

The main approximations being considered by NRAP for simplifying the assessment of CO_2 leakage issues are that (1) CO_2 and brine flow through the well may be treated as quasi-steady-state processes, which is based on an assumption that leakage happens in a relatively short time compared to time scales important to the risk assessment; and (2) CO_2 and water leakage in the well may be decoupled from reservoir flow phenomena caused by well leakage, which is based on an assumption that the leaky well has a minimum impact on the reservoir. The decoupling assumption means that leakage through the well can be described using storage reservoir boundary conditions (e.g., the thermodynamic state variables pressure, saturation, temperature)

at the point where the well intersects the reservoir, and that those conditions at the base of the well are not affected by the leakage process. In this way, the evolution of CO_2 and brine within the reservoir may be evaluated without considering well leakage and similarly, CO_2 and brine leakage up the well can be evaluated without accounting for the effects of leakage on CO_2 and water conditions within the storage reservoir. This is only possible if (1) CO_2 and brine leakage rates are sufficiently small such that thermodynamic conditions within the storage reservoir are not significantly impacted by the leakage, and (2) leakage processes in the well can be approximated as a function of the storage reservoir conditions computed without the effects of well leakage.

This report summarizes analyses performed for a storage reservoir coupled with a leaking well to assess the suitability of the decoupling approximation. In Section 3, a simple example of a coupled leaking well-reservoir system is examined for single-phase flow in which the only coupling effect is pressure loss as a result of flow in the reservoir to the well. In Section 4, process-level flow simulations are described and used to examine the flow behavior of coupled well-reservoir systems for well leakage conditions. The simulations include three-phase (CO_2-rich supercritical fluid, H_2O-rich liquid, and CO_2-rich gas), three-component (CO_2, H_2O, and NaCl) effects. In addition to direct coupling effects, transient flow effects and the influence of the shale caprock are also examined. In Section 5, physics-based reduced-order models (PROMs) are developed for steady-state CO_2 and H_2O leakage through wells from the process-level flow simulations. Section 6 presents alternative PROMs for addressing various issues identified in this report. The Appendix contains previously undocumented PROMs developed for the Generation 1 risk assessment.

3. AN EXAMPLE OF WELL LEAKAGE COUPLED WITH RESERVOIR FLOW

A simple example is presented here to illustrate how coupling between the reservoir and leakage through a well may or may not be important. In this example, a reservoir contains supercritical carbon dioxide exclusively within a thick layer above an aquifer. Significant flow processes in the reservoir are limited to the single-phase CO_2 layer in response to leakage through a well. Furthermore, the reservoir is sufficiently large such that any significant flow induced by the leakage occurs within a zone far from any reservoir boundaries. We make some additional approximations that the density and viscosity of supercritical CO_2 are constant within the storage reservoir. In addition, a suitable approximation for pressure and temperature within the well is used in order to estimate how the CO_2 density and viscosity vary during flow up the well, as described below.

Assume that gas flow (with "gas" here meaning CO_2) is spherically symmetrical about a point sink that represents the leaking well at the top of the reservoir (Figure 1).

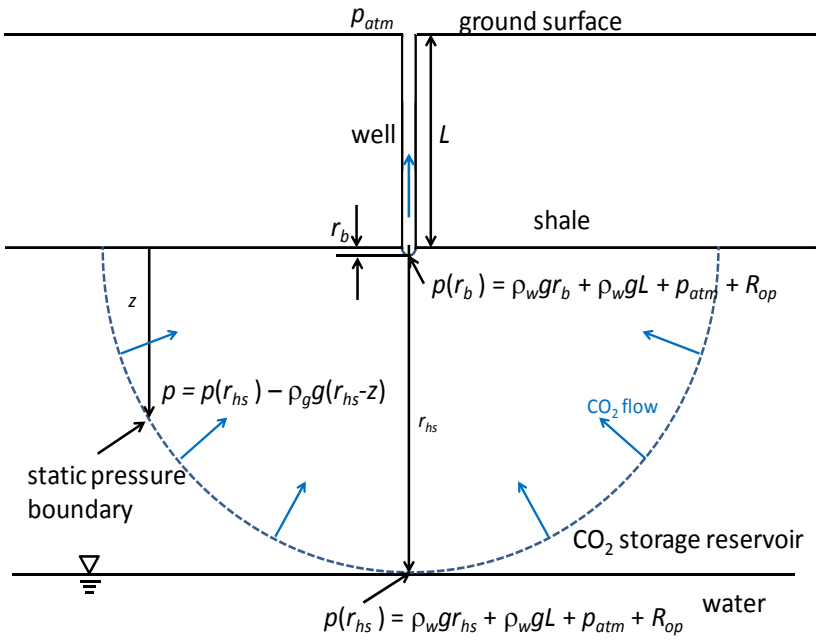

Figure 1: Domain diagram for simple coupled well-leakage-reservoir model.

The top of the reservoir cuts the spherical region in half, thus the flow occurs in a hemi-spherical domain. Darcy's law for steady flow in this situation is,

$$Q_r = 2\pi r^2 \frac{k_r}{\nu_g}\left(\frac{dp}{dr} - \rho_g g\right) \tag{1}$$

where, Q_r is the total-reservoir mass flow rate of gas across any hemisphere centered at the well, k_r the reservoir permeability, p the gas pressure, ρ_g the gas density, ν_g the gas kinematic viscosity, r a radial coordinate centered on the point at the top of the reservoir where the well enters, and g the gravitational acceleration. Because the flow is spherically symmetric, the gradient term in Equation (1) $\left(\frac{dp}{dr} - \rho_g g\right)$ is the same along any radius and for convenience is taken to be a vertical radius.

This equation may be solved by assuming hydrostatic pressure conditions at some (large) distance from the origin, r_{hs}, and some unknown pressure condition at $r = r_b$, the well (or borehole) radius,

$$p(r_b) = \rho_w g r_b + \rho_w g L + p_{atm} + R_{op} + \Delta p \tag{2}$$

$$p(r_{hs}) = \rho_w g r_{hs} + \rho_w g L + p_{atm} + R_{op} \tag{3}$$

where ρ_w is the density of saline water, L the well length, p_{atm} atmospheric pressure, and R_{op} any reservoir overpressure that may have been generated by CO_2 injection. The term Δp is the variation in pressure (from hydrostatic plus overpressure) caused by well leakage at the base of the well, located at radius (r_b). Integrating Equation (1) and using pressure conditions (2) and (3) give

$$Q_r = \frac{2\pi k_r \{(\rho_w - \rho_g) g h_0 - \Delta p\} r_b}{\nu_g} \tag{4}$$

where the approximation $r_{hs} \gg r_b$ has been used and $h_0 = r_{hs} - r_b \approx r_{hs}$ is the thickness of the gas layer.

The mass flow rate in the well, Q_b, may be similarly evaluated based on Darcy's law:

$$Q_b = \frac{\pi r_b^2 k_b}{\nu_g}\left(\frac{dp}{dz} - \rho_g g\right) \tag{5}$$

where k_b is the permeability in the well. This assumes that Darcy flow is valid within the well where flow rates may be high. This may be integrated using Equation (2) for pressure at the base of the borehole and p_{atm} at the top of the borehole, resulting in,

$$Q_b = \frac{\pi r_b^2 k_b \{(\rho_w - \overline{\rho_g}) g L + R_{op} + \Delta p\}}{\overline{\nu_g} L} \tag{6}$$

where

$$\overline{\rho_g} = \int_0^L \rho_g \, dz \tag{7}$$

$$\overline{\nu_g} = \int_0^L \nu_g \, dz \tag{8}$$

Because Q_r and Q_b must be equal under steady-state conditions, Equations (4) and (6) may be solved for Δp

$$\Delta p = \frac{2k_r\overline{v_g}L\{(\rho_w - \rho_g)gh_0\} - r_b k_b v_g\{(\rho_w - \overline{\rho_{sg}})gL + R_{op}\}}{2k_r\overline{v_g}L + r_b k_b v_g} \tag{9}$$

which, after substituting into (6) gives

$$Q_b = \frac{\pi r_b^2 k_b\{(\rho_w - \overline{\rho_g})gL + R_{op}\}}{\overline{v_g}L}\left\{\frac{1 + \frac{(\rho_w - \rho_g)gh_0}{(\rho_w - \overline{\rho_g})gL + R_{op}}}{1 + \frac{r_b k_b v_g}{2k_r\overline{v_g}L}}\right\} \tag{10}$$

The leading term in Equation (10) is the uncoupled well leakage formula, (i.e., Equation (6) with $\Delta p = 0$), which means that all coupling is contained within the term inside the large braces. Notice that the well-reservoir interaction term must be approximately 1 for the assumption of decoupling. We can immediately see that the only way coupling can significantly increase the flow as compared with the uncoupled behavior is through a CO_2 thickness in the reservoir, h_0, that is large in comparison with the well depth, L, which is unlikely. The potential for a large coupling effect requires that well permeability be sufficiently large relative to the reservoir permeability to make the term,

$$\frac{r_b k_b v_g}{2k_r\overline{v_g}L} \gg 1 \tag{11}$$

In that case, it is possible for coupling to significantly reduce the leakage.

The viscosity ratio ($\overline{v_g}\,/v_g$) is estimated to be ~ 4. This means that for significant coupling,

$$\frac{k_b}{k_r} \sim \frac{8L}{r_b} \tag{12}$$

For typical well dimensions of L ~ 1500 m and r_b ~ 0.05 m, we expect that coupling is important when

$$\frac{k_b}{k_r} \sim 10^5 \tag{13}$$

Reservoirs suitable for CO_2 injection are typically limited to permeability levels greater than 0.01 darcies (see Section 4.4). Given this as a lower bound for reservoir permeability, Equation (13) suggests that significant coupling requires a well with a permeability of 1000 darcies or more. As well permeability increases, the significance of coupling impacts on well leakage are expected to increase. Coupling will likely have a significant impact for completely open wellbores; however, the analyses presented here only apply to well leakage that occurs as a Darcy-flow process, while leakage through open wellbores involves other flow processes (Pan et al., 2011). Although this example for single-phase flow provides some guidance concerning reservoir-well coupling, multiphase flow effects have been found to have a significant role in well-leakage phenomena, as discussed below.

4. NUMERICAL MODEL OF WELL LEAKAGE COUPLED WITH THE STORAGE RESERVOIR

We developed a numerical model of well leakage coupled with a storage reservoir as a basis for understanding coupled effects of reservoir flow and well leakage and to help develop a reduced-order model for these processes. The numerical model was conducted using TOUGH2-ECO2M, a numerical simulator specifically developed for mixtures of water, sodium chloride, and CO_2, including super- and sub-critical conditions, and phase change between liquid and gaseous CO_2 (Pruess, 2011a).

4.1 MODELING DOMAIN AND NUMERICAL GRID

The modeling domain was set up as a radially-symmetric system with the well at the center of the domain as shown in Figure 2. The overall domain has a 2-km radius and 1600 m in depth. A 100-m thick permeable reservoir occupies the base of the domain. Above the reservoir is an impermeable shale layer with a 5-cm radius well at the center from 1500-m depth to the ground surface; the well does not penetrate through the storage reservoir. A radial grid with refined gridding around the well and along the top of the reservoir was found necessary to correctly model the coupled reservoir-well problem as shown in Figure 3. In particular, grid refinement is essential within the reservoir just below the well. The vertical cell dimensions are as small as 1 mm immediately below the well. Tests with a coarser grid using a cell with a vertical dimension of 5 m immediately below the well resulted in well leakage being excessively sensitive to reservoir properties. This occurs because of the poor approximation to spherically-symmetric radial flow with such a coarse grid. Some grid refinement is also seen within the shale near the ground surface, which is present for future studies concerning CO_2 releases from a leaking well into a fresh-water aquifer.

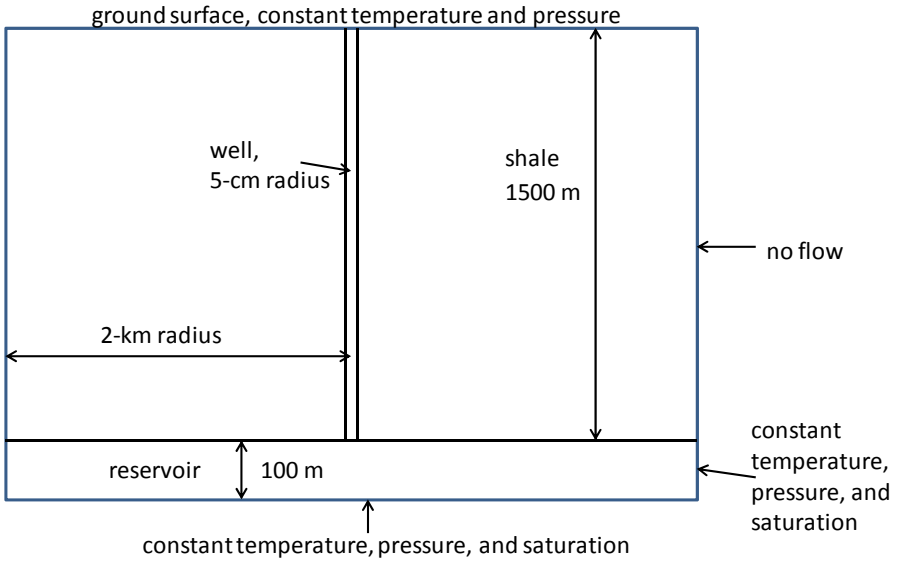

Figure 2: Model domain and boundary conditions.

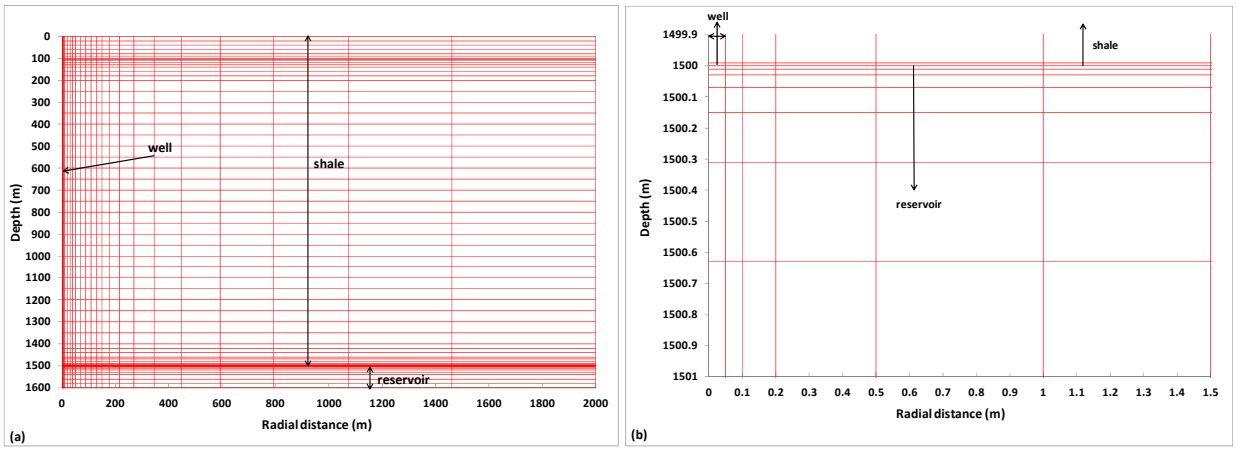

Figure 3: Numerical grid. (a) entire domain; (b) detail near well-reservoir interface.

4.2 BOUNDARY AND INITIAL CONDITIONS

The boundary conditions at the 2-km radial boundary were assigned as constant pressure, saturation, and temperature conditions for the reservoir and no-flow conditions for the shale (Figure 2). Constant thermodynamic conditions were imposed at the upper and lower boundaries. Because there is no specific reservoir CO_2 injection geometry that can be applied, or other known reservoir conditions, the initial conditions were specified as a CO_2-water system under capillary-gravity equilibrium in the reservoir, with the overlying shale and well saturated with water. Initial saturations are uniform in the radial direction.

The capillary-gravity equilibrium initial condition was instituted by first equilibrating the reservoir with an approximate capillary-gravity saturation distribution of CO_2 and water within the storage reservoir. The well permeability is set to the value of the shale permeability for the equilibration calculations. A first equilibration is performed by assigning a no-flow boundary condition at the lateral boundary within the reservoir so that equilibration can be reached more quickly. After the first equilibration, a final equilibration calculation is performed by assigning a constant thermodynamic boundary condition to check the stability of the initial condition.

Three saturation cases were investigated, having average CO_2 saturations of 0.01, 0.2, and 0.5 which correspond to CO_2 layer thicknesses of about 3 m, 30 m, and 80 m, respectively, within the 100-m thick storage reservoir, as shown in Figure 4. The CO_2 layer is not sharply defined but is gradational between a higher CO_2 saturation at the top of the reservoir and a lower CO_2 saturation at the bottom of the reservoir. Therefore, the position of the CO_2-water interface was identified by taking the average of the CO_2 saturation at the top and bottom of the reservoir and then finding the midpoint between the grid cells with CO_2 saturations that bound this value. Disturbances in the strictly vertical capillary-gravity equilibrium profiles can be seen at the far radial boundary, but these are about 2 km from the well and are stable over time, so the impact on well leakage is minimal. Saturations at the top of the reservoir where the formation interfaces with the well have CO_2 saturations of 0.411 in Figure 4(a), 0.655 in Figure 4(b), and 0.682 in Figure 4(c). With a residual water saturation of 0.3, these cases have water saturations that are 0.289, 0.045, and 0.018, saturation units above residual, respectively. This translates into decreasing water mobility for the higher CO_2 saturation cases. In addition to the three saturation conditions, five reservoir pressure conditions were also investigated. The pressures are expressed

in terms of overpressure, caused by CO_2 injection, relative to hydrostatic conditions; these have values of 0.03, 0.7, 1, 1.3, and 5.2 MPa.

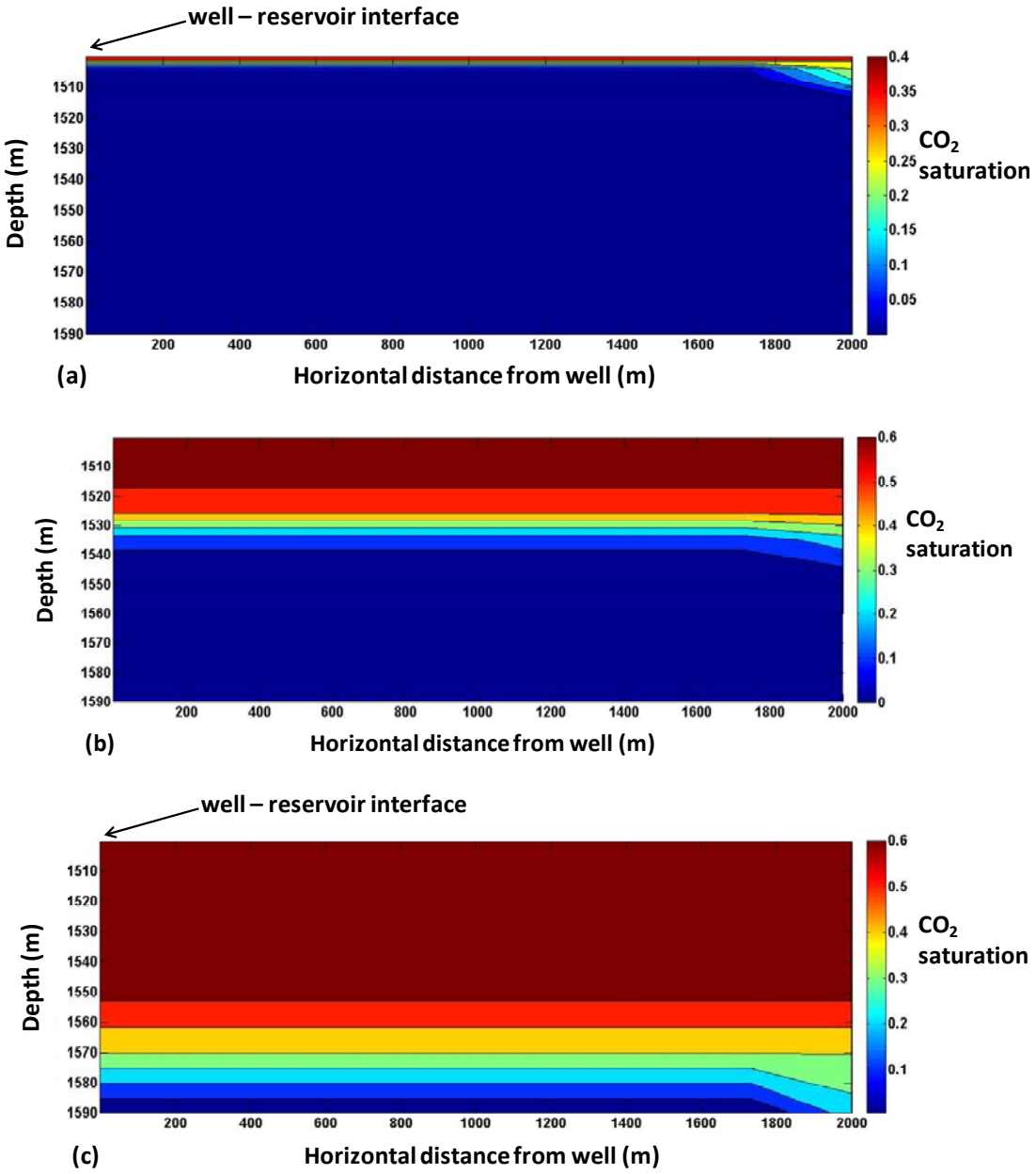

Figure 4: Initial reservoir saturations distributions: (a) average CO_2 saturation 0.01; (b) average CO_2 saturation 0.2; and (c) average CO_2 saturation 0.5.

4.3 CASES INVESTIGATED

The cases investigated are summarized in Table 1. All sets of cases, for example rg4–rg18, consist of 15 combinations associated with three reservoir permeabilities and five well permeabilities (Table 1), except for the set rg64–rg75. The set rg64–rg75 only has 12 cases because the calculations with high reservoir overpressure were numerically unstable for cases

with the highest well permeability, 1,000 darcies. Note that cases rg79–rg93, with higher shale permeabilities, are discussed in this report only in terms of a comparison with cases rg49–rg63.

Within each set, the lowest number corresponds to the combination having the lowest well and reservoir permeabilities, e.g., rg4 has a well permeability of 0.1 darcies and a reservoir permeability of 0.01 darcies. Increments in the case number correspond with increments first in the reservoir permeability cases before incrementing the well permeability, i.e., rg5 and rg6 both have the same well permeability as rg4, 0.1 darcies, and reservoir permeabilities of 0.1 and 1 darcies, respectively. The next case, rg7, has a well permeability of 1 darcy and a reservoir permeability of 0.01 darcies, and so forth as shown in Table 2.

Table 1: Cases investigated

Case identifiers	Average CO_2 saturation in reservoir, S_g	CO_2 layer thickness at top of reservoir, T (m)	Reservoir overpressure, R_{op} (MPa)	Shale permeability, k_s (darcies)	Total number of cases
rg4–rg18	0.5	80	0.03	impermeable	15
rg19–rg33	0.01	3	0.74	impermeable	15
rg34–rg48	0.2	30	0.99	impermeable	15
rg49–rg63	0.5	80	1.3	impermeable	15
rg64–rg75	0.5	80	5.2	impermeable	12
rg79–rg93	0.5	80	1.3	10^{-7}	15

Table 2: Permeability combinations

Case identifiers	Well permeability, k_b (darcies)	Reservoir permeability, kr (darcies)	Well to reservoir permeability ratio
rg4, rg19, rg34, rg49, rg64, rg79	0.1	0.01	10
rg5, rg20, rg35, rg50, rg65, rg80	0.1	0.1	1
rg6, rg21, rg36, rg51, rg66, rg81	0.1	1	0.1
rg7, rg22, rg37, rg52, rg67, rg82	1	0.01	100
rg8, rg23, rg38, rg53, rg68, rg83	1	0.1	10
rg9, rg24, rg39, rg54, rg69, rg84	1	1	1
rg10, rg25, rg40, rg55, rg70, rg85	10	0.01	1,000
rg11, rg26, rg41, rg56, rg71, rg86	10	0.1	100
rg12, rg27, rg42, rg57, rg72, rg87	10	1	10
rg13, rg28, rg43, rg58, rg73, rg88	100	0.01	10,000
rg14, rg29, rg44, rg59, rg74, rg89	100	0.1	1,000
rg15, rg30, rg45, rg60, rg75, rg90	100	1	100
rg16, rg31, rg46, rg61, rg91	1,000	0.01	100,000
rg17, rg32, rg47, rg62, rg92	1,000	0.1	10,000
rg18, rg33, rg48, rg63, rg93	1,000	1	1,000

4.4 PROPERTIES USED FOR THE SIMULATIONS

The hydrogeologic properties used for the simulations are given in Table 3. All properties are held constant for the various simulations using a given initial condition except reservoir and well permeabilities. All permeabilities used are isotropic. The shale formation is assumed to be essentially impermeable in these simulations (i.e., with a 10^{-18} darcies permeability), but is included in the model because it exchanges heat with the leaking CO_2. Because the well leakage investigated here concerns flow outside of the casing that is in contact with the surrounding formation, fluid interactions between well leakage and shale are possible. Changing the shale permeability to a more realistic value (10^{-7} darcies) had a non-negligible effect on leakage rates

in the well, particularly in the cases with low-permeability wells. We assumed the impermeable case in this study to focus on well-reservoir interactions. The effect of shale permeability will require a more detailed investigation in the future. Even though the shale effectively behaved essentially as a no-flow boundary for CO_2 and water, it performed a more active role with respect to thermal processes in the well.

Table 3: Simulation properties

Property	Values
porosity, all rock types and well	0.264
permeability, shale (darcies)	impermeable
permeability, reservoir (darcies)	0.01, 0.1, 1
permeability, well (darcies)	0.1, 1, 10, 100, 1,000
pore compressibility, all rock types and well (Pa^{-1})	4.9×10^{-10}
van Genuchten α (capillary strength), all rock types and well (Pa^{-1})	1.5×10^{-4}
van Genuchten m (pore-size distribution index), all rock types and well	0.457
residual water saturation	0.3
residual gas saturation	0.25

Capillary pressure, p_c, (gas-phase pressure minus aqueous-phase pressure) is based on the van Genuchten relationship given by the following:

$$p_c = \frac{1}{\alpha}\left(S_{wn}^{-\frac{1}{m}} - 1\right)^{1-m} \tag{14}$$

$$S_{wn} = \frac{S_w - S_{wr}}{1 - S_{wr}} \tag{15}$$

where S_w and S_{wr} are the water saturation and residual water saturation, respectively.

Relative permeability functions are van Genuchten for the aqueous phase and Corey for the gas phase given by

$$k_{rw} = \sqrt{S_{wn}}\left\{1 - \left(1 - S_{wn}^{\frac{1}{m}}\right)^{m}\right\}^2 \tag{16}$$

$$k_{rg} = \left(1 - \hat{S}_{wn}\right)^2\left(1 - \hat{S}_{wn}^2\right) \tag{17}$$

$$\hat{S}_{wn} = \frac{S_w - S_{wr}}{1 - S_{wr} - S_{gr}} \tag{18}$$

where S_{gr} is the residual gas saturation.

For well-leakage problems, there is the possibility of three-phase conditions in which CO_2 liquid, CO_2 gas, and aqueous phases are all present within a single grid cell. Where three-phases occur, both CO_2 phases are described by the gas relative permeability function for the simulations reported here. Options exist for three-phase relative permeability functions in TOUGH2-ECO2M (Pruess, 2011a), but these have not been used for these calculations. In fact, very few problems at

steady-state were found to have three-phase conditions, and in those few cases where three phases do appear, they are limited to one cell within the well near the phase-transition point.

Well leakage in this report refers to leakage outside the well casing through a permeable material in which flow processes can be described by Darcy's law. This is to be distinguished from a leak inside the casing associated with a well blowout in which flow is occurring through essentially an open wellbore. Leakage outside the casing is occurring through a damaged zone typically containing degraded cement, damaged rock, and drilling fluids (Celia et al., 2011). A significant problem for assigning well parameters is that little is known about what ranges of hydrogeologic parameters are representative for a leaking well condition. Celia et al. (2011) used the results from analysis of Watson and Bachu (2008, 2009) to identify a wide range of well permeabilities from 8×10^{-2} to 10 darcies as having the highest likelihood of well leakage. Well-leakage analyses for flow outside the casing reported by Cihan et al. (2012) used a range of well permeabilities from 1 to 1,000 darcies. Because coupling effects between well-leakage and reservoir flow are expected to be more significant for high well permeabilities, this study considers a well permeability range of 0.1 to 1,000 darcies.

While the range of permeabilities for the well and reservoir span representative ranges, many of the other parameters that are used as single values can only be considered as possible parameter values and a full parameter investigation should vary these properties over representative ranges. The reservoir permeability range is based on Friedman (2007), who listed 12 current and pending large CO_2 injection projects, identifying Sleipner as having the highest-permeability reservoir and In Salah as having the lowest. The reservoir permeability at Sleipner is 3 darcies (Audigane et al., 2007); at In Salah, it is 0.01 darcies (BP, 2012). Capillary pressure and relative permeability for CO_2 water systems in geologic materials is presented in Bachu and Bennion (2008), who show that relative permeability curves are generally nonlinear, but become closer to linear with a reduction in the CO_2-water interfacial tension. The van Genuchten characteristics are similar to values used for geologic CO_2 storage by Zhou et al. (2008).

4.5 FLOW BEHAVIOR

There are two categories of flow behavior resulting from well leakage. In the first category, H_2O flow in the well is caused entirely by H_2O dissolved in the CO_2; the aqueous phase in the reservoir does not enter the well directly. H_2O moving up the leaking well is fresh; no salts from the storage reservoir water can enter because all H_2O enters the well dissolved in the CO_2, and salts do not partition into CO_2. In the second category, at least some water from the reservoir flows directly into the well, in addition to H_2O carried as a dissolved phase by the CO_2, which appears to be associated with upconing in the reservoir. Furthermore, some cases in the second category show a significant secondary transient in the CO_2 and water flow in the reservoir is induced by leakage up the well that is not found in the first category. This is called a secondary transient, to distinguish it from the primary transient, which occurs in all leaking wells, which results from the displacement of water by CO_2 in the leaking well. These flow features are investigated only for the well geometry identified in Section 4.1, in which the well penetrates to the storage reservoir but not into the storage reservoir. The flow behavior discussed here could be expected to be different if the well were to partially or fully penetrate the storage reservoir. Another aspect of this study that can affect the results is that a stable reservoir CO_2-aqeuous phase stratification is established in the reservoir (without any influence of well leakage) before leakage is initiated. In a real system, it may be expected that well leakage would initiate as soon

as the tip of the CO_2 plume advances towards the well, which could also influence the well-leakage and reservoir-flow responses.

These two types of flow behavior are related to the thickness of the CO_2 layer in the storage reservoir. The first category is referred to as "thick-layer behavior" and the second category as "thin-layer behavior" because the different flow categories tend to be distinguished on the basis of the CO_2-layer thickness. However, the different flow categories are not distinguished entirely by CO_2 layer thickness; they also show some dependence on the well-to-reservoir permeability ratio and the reservoir-overpressure-to-buoyancy ratio. A more detailed discussion of the dependence of flow behavior on these parameters is given in Section 4.5.3. The effect of the CO_2 layer thickness on flow behavior is twofold; (1) a thick CO_2 layer necessarily generates a higher CO_2 saturation at the top of the reservoir (lower aqueous saturation) and, therefore, a lower aqueous permeability just below the well as compared with a thin CO_2 layer; and (2) a thick CO_2 layer displaces high aqueous saturation conditions below the CO_2 layer further from the well than a thin CO_2 layer. Both of these factors have a qualitative impact on how H_2O moves into the well. Thick-layer behavior means that H_2O enters the well only as a dissolved component in the supercritical CO_2 because the conditions preclude bulk aqueous flow into the well, whereas for thin-layer behavior, the aqueous phase from the storage reservoir can flow into the well. For thick-layer behavior, H_2O dissolved in the supercritical CO_2 exsolves during flow up the well creating a bulk aqueous phase in the well. Furthermore, the magnitude of the supercritical CO_2 pressure gradient decreases with depth in the well as a result of increasing CO_2 saturation and therefore, increasing effective permeability to CO_2. Because capillary pressures over much of the well are small, the aqueous-phase pressure gradient is approximately the same as that in supercritical CO_2. The trend in the pressure gradient can result in a reversal in the total gradient for the aqueous phase. If the gradient reverses, aqueous-phase flow moves downwards near the base of the well and upwards at locations in the well above the reversal. This behavior is used to distinguish thick-layer versus thin-layer behavior from the simulation output. If aqueous-phase flow is downwards at any location in the well, then the case is categorized as thick-layer; if all aqueous-phase flow in the well is upwards then the case is categorized as thin-layer.

In the descriptions that follow, the fluid system within the well is described by three phases, a supercritical fluid phase, a liquid phase, and a gas phase with three components (CO_2, H_2O, and NaCl). These are shown in Figure 5. The supercritical fluid is a CO_2-rich phase with varying degrees of dissolved H_2O, the liquid phase is H_2O-rich with varying degrees of dissolved NaCl and CO_2, and the gas phase is composed mainly of CO_2 with varying amounts of H_2O. Below the depth where CO_2 transitions to a gas phase, CO_2 exists as a supercritical fluid with some amount of dissolved H_2O. Above the phase-transition point, CO_2 becomes a gas phase along with any H_2O dissolved in the supercritical CO_2. The specific depth where the CO_2 phase transition occurs varies from case to case. In some cases, the aqueous-liquid-phase reverses flow direction near the base of the well and may completely evaporate near the ground surface. Cases with the H_2O-rich liquid flow reversal at the base of the well do not carry any NaCl into the well because NaCl does not partition into the CO_2-rich supercritical fluid. For brevity in the following discussions, the CO_2-rich supercritical fluid with dissolved H_2O will be called "supercritical CO_2" or just "CO_2," the H_2O-rich liquid with dissolved CO_2 and NaCl will be called "water," and the CO_2-rich gas with H_2O vapor will be called "CO_2 gas."

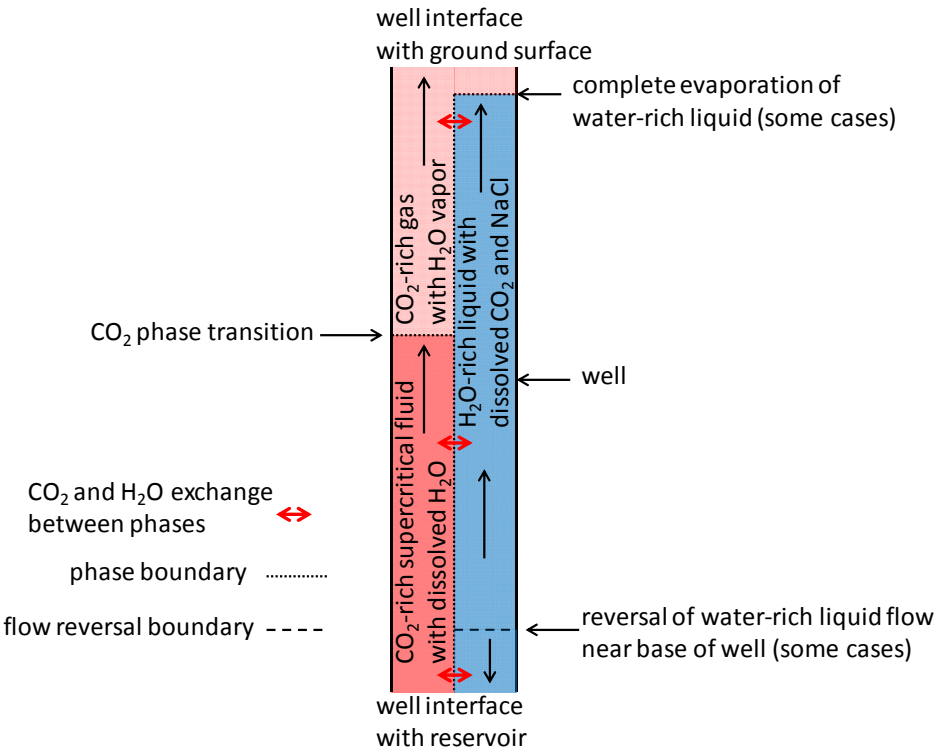

Figure 5: Phases, components, and mass transport during well leakage.

4.5.1 Leakage Flow Behavior from Reservoir with a Thick CO_2 Layer

Given the impermeable nature of the shale in communication with the well, steady-state flow behavior in the well means that the mass flow rates of CO_2 and H_2O along the well are constant over the well depth. As shown in Figure 3, CO_2 moves as a supercritical fluid in the lower part of the well, a gas phase in the upper part of the well, and dissolved in water over much of the well depth. H_2O moves as a dissolved phase in the supercritical CO_2 in the lower part of the well, as a gas phase in the upper part of the well, and as water over much of the well depth. However, the quantity of CO_2 carried in water was found to be negligible in all cases investigated here relative to the quantity of CO_2 moving as a supercritical fluid or gas. As a result, the mass flow rate for CO_2 in the supercritical CO_2 and gas was found to be constant over the well depth at steady state. On the other hand, a significant quantity of the overall H_2O mass flow rate occurs as a dissolved component in the CO_2 supercritical fluid in many of the cases investigated here. The reason H_2O dissolved in CO_2 plays an important role is that at the base of the well (i.e., the top of the reservoir) water has been displaced by CO_2, thus severely restricting water mobility. As a result, H_2O cannot readily flow into the well as a bulk aqueous phase and enters mainly as a dissolved phase in CO_2 that exsolves from the CO_2 as it moves up the well. Therefore, steady-state flow does not mean that the mass flow rate of water is constant over the borehole depth.

Figure 6(a) shows an example of how H_2O mass flow up the borehole is partitioned between the various phases for case rg53, which has an 80-m thick CO_2 layer, a 1.3 MPa overpressure in the reservoir, along with well and reservoir permeabilities of 1 and 0.1 darcies, respectively. The distinctive aspect of the well leakage used to define thick-layer behavior is that the water flow rate at the base of the well is negative, indicating that water is moving down the well into the reservoir. Flow reversal occurs moving up the well as dissolved H_2O leaves the supercritical CO_2

and liquefies. CO_2 transitions from a supercritical fluid to gas at a depth of about 575 m. At this phase transition, H_2O carried in the supercritical CO_2 also enters the gas phase. H_20 within the well is moving as (1) a dissolved component in the supercritical CO_2 (or as gas-phase H_2O at shallow depths) and (2) water. Typically, both modes of H_2O transport are occurring at any point in the well, although in some cases near the top of the well, H_2O transport occurs exclusively in the gas phase. The total mass flow rate of H_2O is constant over the well depth, as required for steady-state flow conditions. Figure 6(b) shows the CO_2 saturation profile over the well depth and from the bottom of the well to the base of the storage reservoir. The minimum CO_2 saturation occurs at a location close to the CO_2 phase transition, which was found to be true for all cases. The depth of this transition and the degree of CO_2 saturation nonuniformity varies for the different cases. Figure 6(c) shows the pressure depletion caused by flow in the reservoir to the well. A small level of pressure depletion is found, less than 0.002 percent of total reservoir pressure and 0.03 percent of reservoir overpressure. This is a result of the low well permeability (1 darcy) and moderate reservoir permeability (0.1 darcies). Pressure depletion in the reservoir would also be greater if the shale permeability was modeled using a more realistic value.

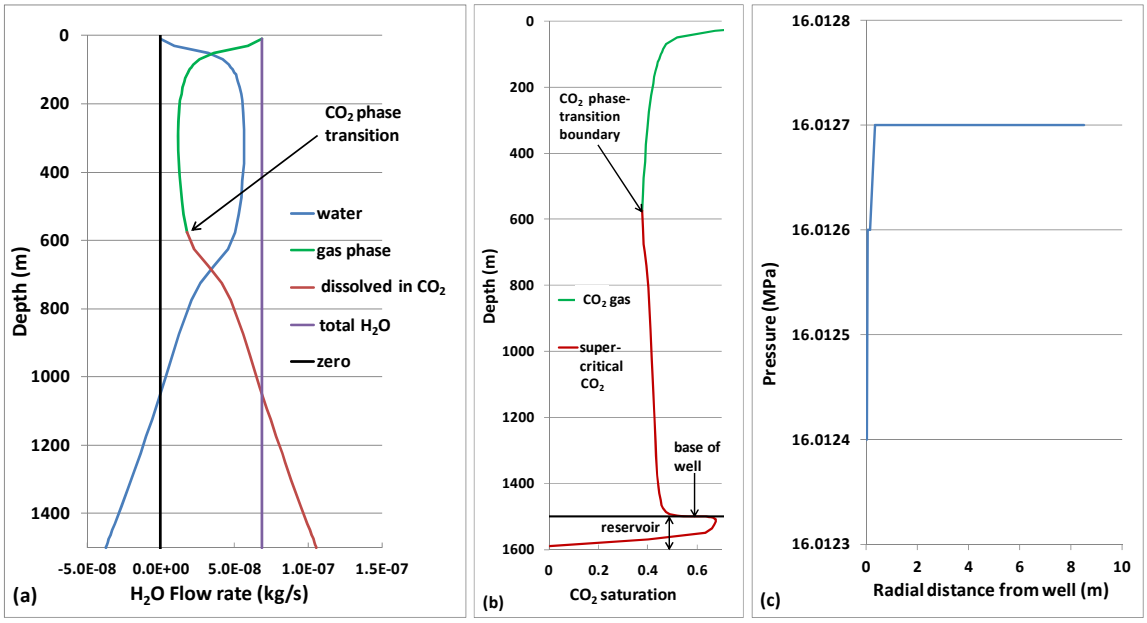

Figure 6: Steady-state results for leakage case rg53 (k_b = 1 darcy, k_r = 0.1 darcies, S_g = 0.5, R_{op} = 1.3 MPa). (a) H_2O mass flow rate along well; (b) CO_2 phase saturation along well; (c) radial pressure profile along top of reservoir.

The perturbation in reservoir saturations is shown in Figure 7. The depletion in the CO_2 saturation locally near the well is mainly a result of the water flow down the well into the reservoir. This type of CO_2 depletion has also been found for some thin-layer cases without the downward flow of water at the base of the borehole; however, the depletion is much weaker.

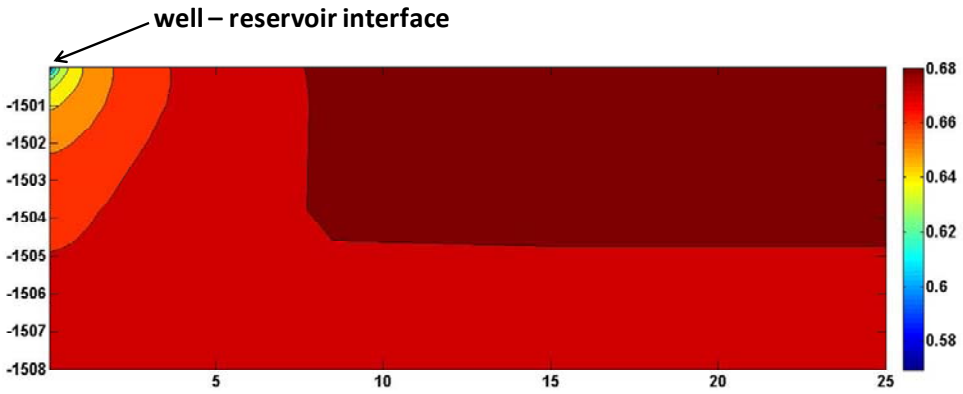

Figure 7: CO_2 saturation contours for case rg53 (k_b = 1 darcy, k_r = 0.1 darcies, S_g = 0.5, R_{op} = 1.3 MPa).

The transient response for rg53 is shown in Figure 8. This is a primary transient caused by the mechanics of CO_2 displacement of water in the well. Breakthrough occurs in just a few years, but the transient lasts for about 100 years before reaching steady-state conditions. Figure 9 shows several primary transients for thick-layer cases, which indicates that the duration of the primary transient is mainly a function of well permeability. Transients for low-permeability wells (0.1 darcies) last for about 1,000 years, and each increase in permeability by a factor of 10 roughly corresponds to a decrease in the transient period by a factor of 10. Some instability is seen at steady state for the higher-overpressure case, rg72. A characteristic of primary transient flow is that the CO_2 mass flow rate peaks at the steady-state condition. Therefore, a steady-state model will conservatively overestimate CO_2 mass flow rates during the primary transient period.

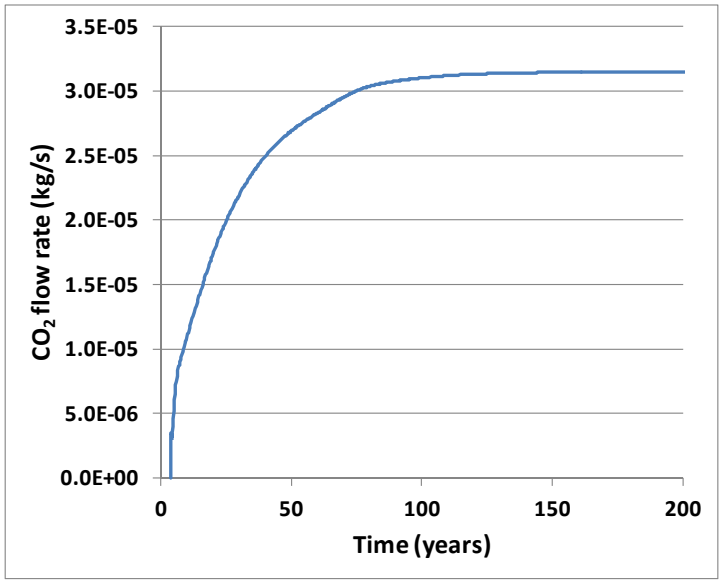

Figure 8: Primary transient well leakage at ground surface for rg53 (k_b = 1 darcy, k_r = 0.1 darcies, S_g = 0.5, R_{op} = 1.3 MPa).

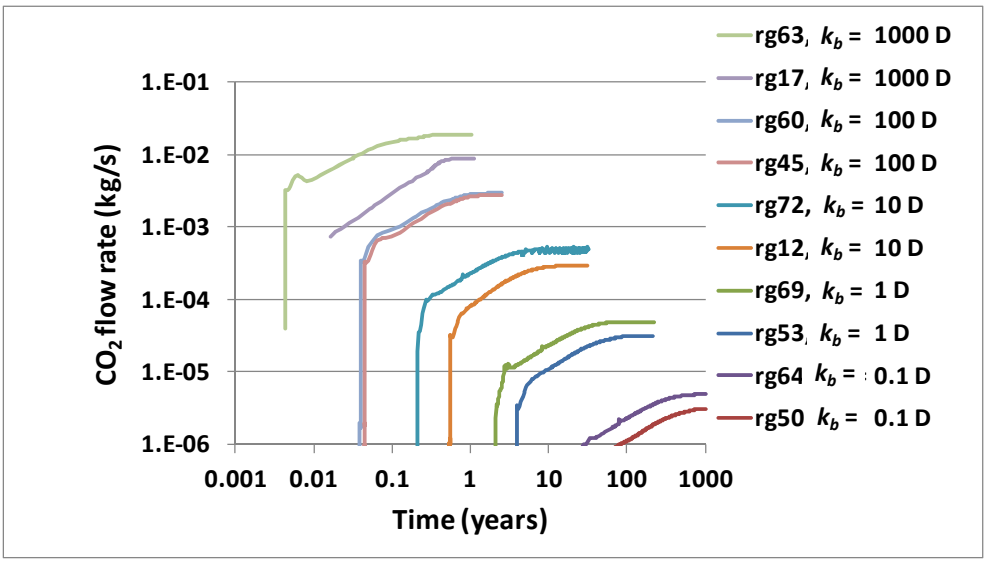

Figure 9: Primary transient well leakage at surface for thick-layer cases. Tables 2 and 3 present complete definitions of the different cases.

4.5.2 Leakage Flow Behavior from Reservoir with a Thin CO_2 Layer

As discussed in Section 4.5, thick-layer versus thin-layer behavior is distinguished based on the direction of water flow in the well. For a thin-layer response, water flow in the well must be upwards at all locations for steady-state conditions. This means that water in the well carries at least some salt present in water within the storage reservoir. However, because water may also be transported as a dissolved component in the supercritical CO_2, the water may be diluted by water released from the supercritical CO_2. Figure 10 shows case rg46 with weak thin-layer behavior. This case has a 30-m thick CO_2 layer and a 0.99 MPa overpressure in the reservoir and well, and reservoir permeabilities of 1,000 and 0.01 darcies, respectively. In this case, the water flow is barely positive at the base of the well and increases with decreasing depth (Figure 10a); most of the water in the well is carried in as dissolved H_2O in the CO_2. CO_2 saturation within the well is fairly constant until near the surface, but differs significantly from CO_2 saturations in the reservoir immediately below the well (Figure 10(b)). Pressure depletion is relatively large, with 4 percent depletion of total reservoir pressure and 64 percent depletion of overpressure at the well (Figure 10(c)). Strong pressure depletion results from high well permeability (1,000 darcies) and low reservoir permeability (0.01 darcies). The saturation distribution in the reservoir at 1,000 years in Figure 10(d) shows the characteristic tilting of the contour lines for a thin-layer case. The saturation distribution continues to adjust out to 19,000 years (Figure 10(e)). Transient behavior in Figure 10(f) shows the initial primary transient in which the CO_2 flow rate is increasing, followed by a slight decrease at long times caused by the secondary transient induced in the reservoir. We investigate these long transients because they are potential sources of error when attempting to represent well leakage using steady-state models.

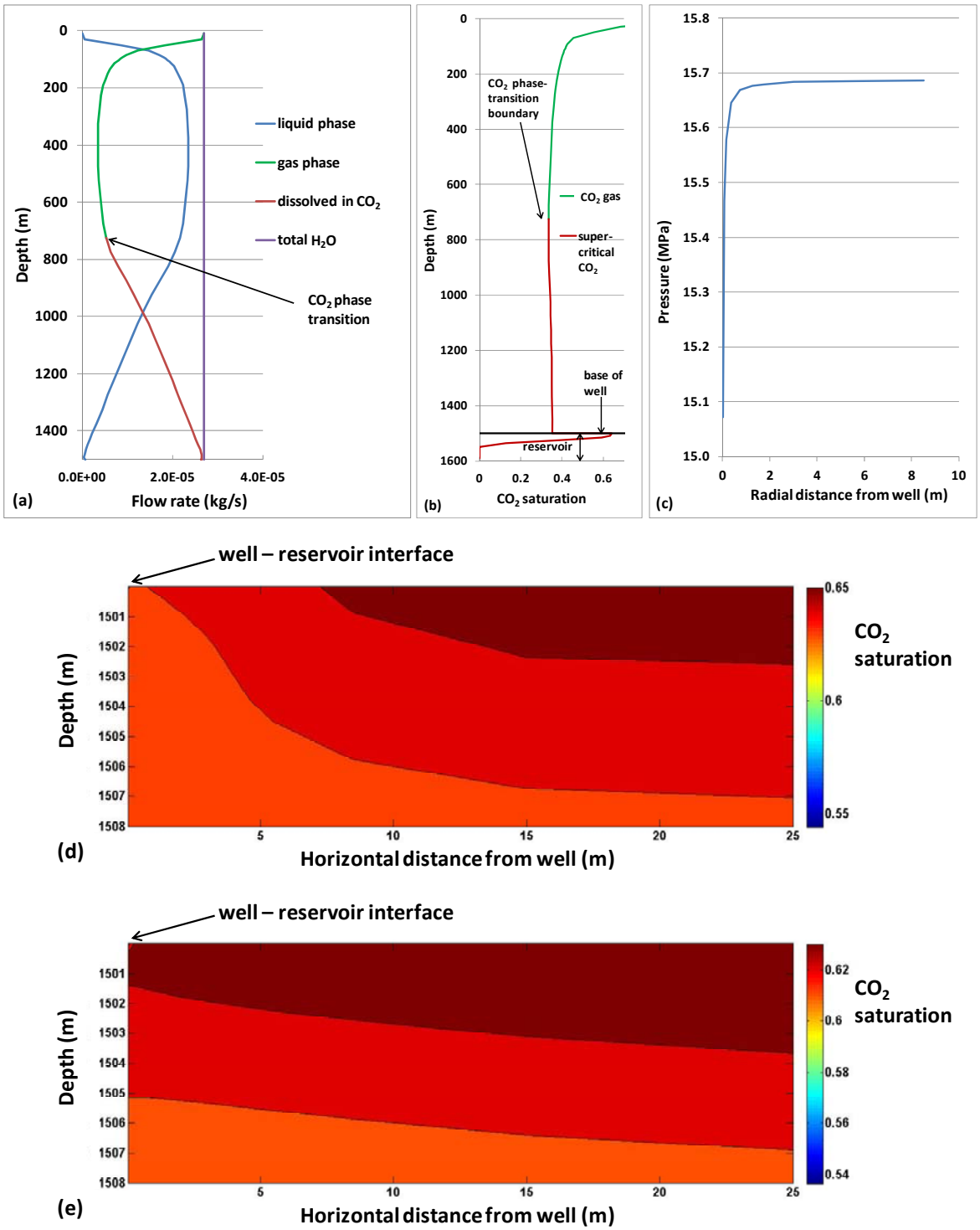
(a)
Depth (m)
Flow rate (kg/s)
liquid phase
gas phase
dissolved in CO2
total H2O
CO2 phase transition
(b)
Depth (m)
CO2 saturation
CO2 phase-transition boundary
CO2 gas
super-critical CO2
base of well
reservoir
(c)
Pressure (MPa)
Radial distance from well (m)
well – reservoir interface
(d)
Depth (m)
Horizontal distance from well (m)
CO2 saturation
well – reservoir interface
(e)
Depth (m)
Horizontal distance from well (m)
CO2 saturation

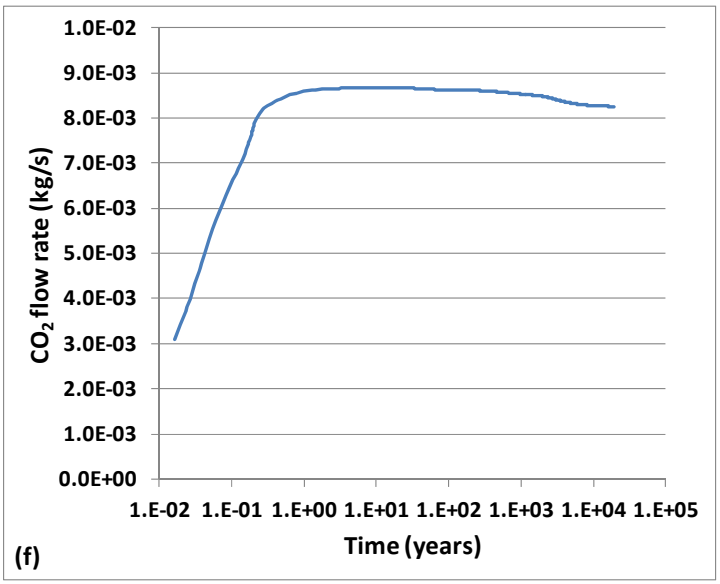

Figure 10: Results for leakage case rg46 (k_b = 1,000 darcy, k_r = 0.01 darcies, S_g = 0.2, R_{op} = 0.99 MPa). Weak thin-layer behavior. (a) H_2O mass flow rate at 1,000 years; (b) CO_2 phase saturation at 1,000 years; (c) radial pressure profile along top of reservoir at 1,000 years; (d) saturation contours at 1,000 years; (e) saturation contours at 19,000 years; (f) transient well leakage at ground surface.

Figure 11 shows case rg22 with intermediate thin-layer behavior. This case has a 3-m thick CO_2 layer and a 0.74 MPa overpressure in the reservoir and well and reservoir permeabilities of 1 and 0.01 darcies, respectively. A substantial fraction of the total H_2O flow rate enters the well as water (Figure 11(a)). The saturation distribution is flatter and saturations in the reservoir below the well are closer to those at the base of the well (Figure 11(b)). The pressure depletion is low, 0.6 percent of reservoir overpressure, as expected for a case with a 1 darcy well and a 0.1 darcies reservoir (Figure 11(c)). The saturation distribution in the reservoir at 1,000 years in Figure 11(d) shows tilting of the contour lines; in this case the higher levels of CO_2 saturation are displaced away from the well. Changes in the saturation distribution after 95,000 years can be seen in Figure 11(e). Transient behavior in Figure 11(f) shows the initial primary transient in which the CO_2 flow rate is increasing, followed by a moderate (~20 percent) decrease at long times (~100,000 years) caused by the secondary transient induced in the reservoir.

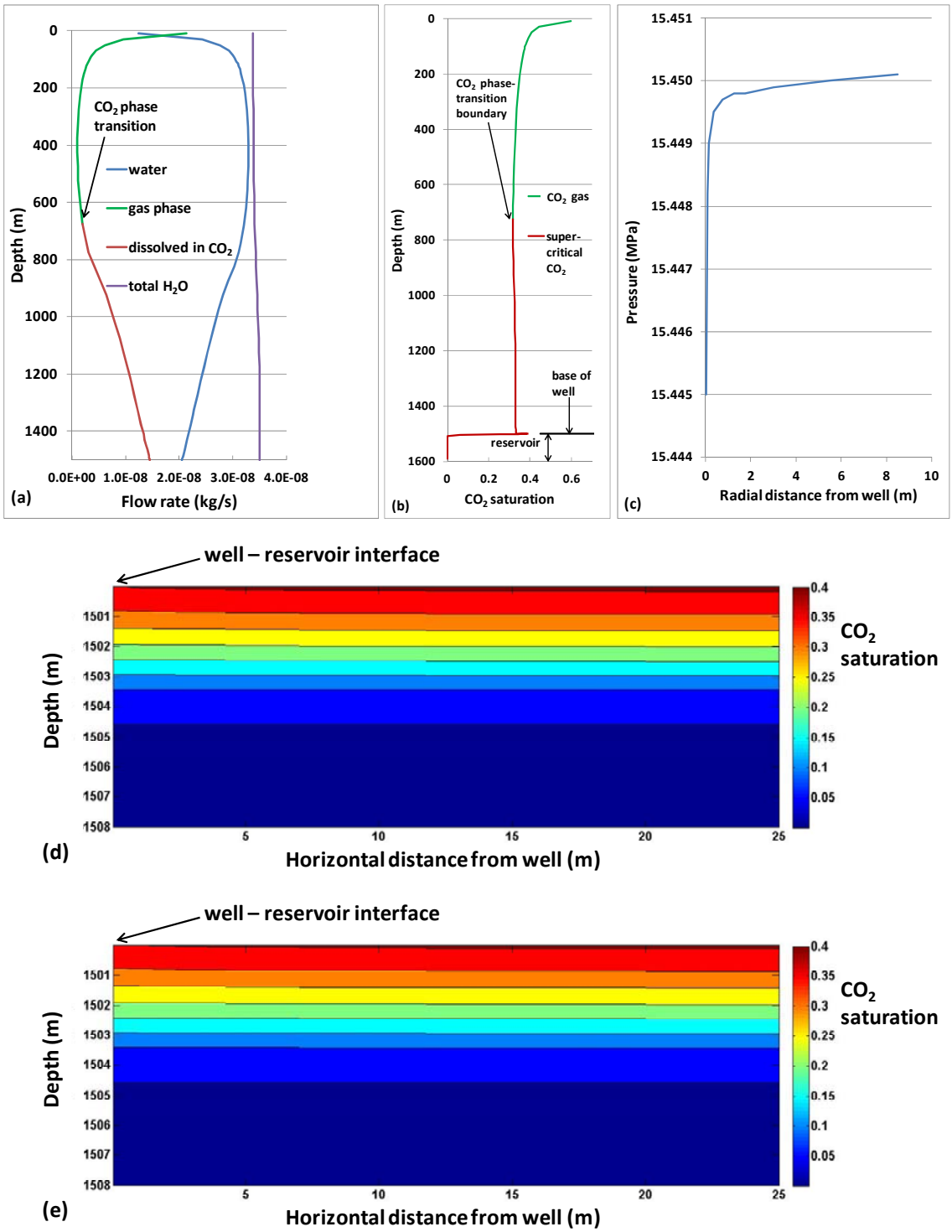
(a)
Depth (m)
Flow rate (kg/s)
0.0E+00 1.0E-08 2.0E-08 3.0E-08 4.0E-08
CO_2 phase transition
water
gas phase
dissolved in CO_2
total H_2O
(b)
Depth (m)
CO_2 saturation
CO_2 phase-transition boundary
CO_2 gas
super-critical CO_2
base of well
reservoir
(c)
Pressure (MPa)
Radial distance from well (m)
(d)
well – reservoir interface
Depth (m)
Horizontal distance from well (m)
CO_2 saturation
(e)
well – reservoir interface
Depth (m)
Horizontal distance from well (m)
CO_2 saturation

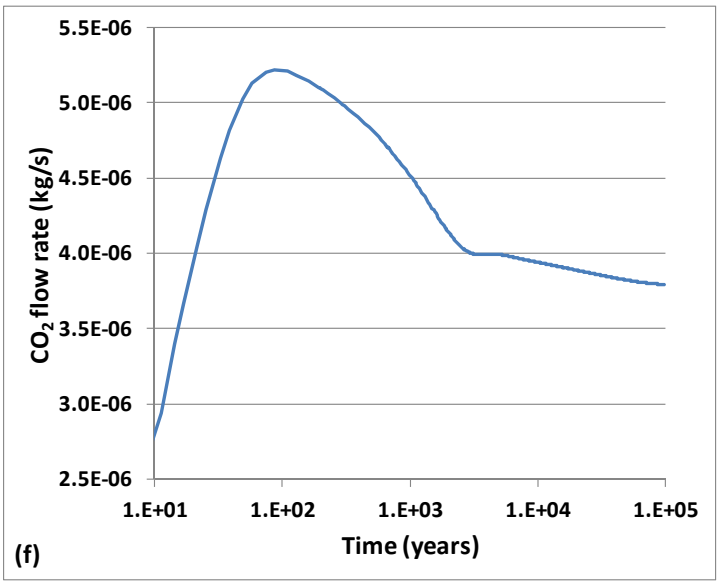

Figure 11: Results for leakage case rg22 (k_b = 1 darcy, k_r = 0.01 darcies, S_g = 0.01, R_{op} = 0.74 MPa). Intermediate thin-layer behavior. (a) H_2O mass flow rate at 1,000 years; (b) CO_2 phase saturation at 1,000 years; (c) radial pressure profile along top of reservoir at 1,000 years; (d) saturation contours at 1,000 years; (e) saturation contours at 95,000 years; (f) transient well leakage at ground surface.

Figure 12 shows case rg31 with strong thin-layer behavior. This case has a 3-m thick CO_2 layer and a 0.74 MPa overpressure in the reservoir and well, and reservoir permeabilities of 1,000 and 0.01 darcies, respectively. Nearly all H_2O enters the well as water (Figure 12(a)). The saturation distribution is flat, and saturations in the reservoir below the well are close to those at the base of the well (Figure 12(b)). Pressure depletion is significant at 19 percent of overpressure at the well (Figure 12(c)). As for case rg46 (Figure 10), strong pressure depletion results from high well permeability (1,000 darcies) and low reservoir permeability (0.01 darcies). The saturation distribution in the reservoir at 1,000 years in Figure 12(d) shows tilting of the contour lines; in this case, the higher levels of CO_2 saturation are even more strongly displaced away from the well. Changes in the reservoir saturation distribution are seen in Figure 12(e) at 256,000 years. Transient behavior shows the initial primary transient in which the CO_2 flow rate is increasing, followed by a strong (~98 percent) decrease at long times caused by the secondary transient induced in the reservoir.

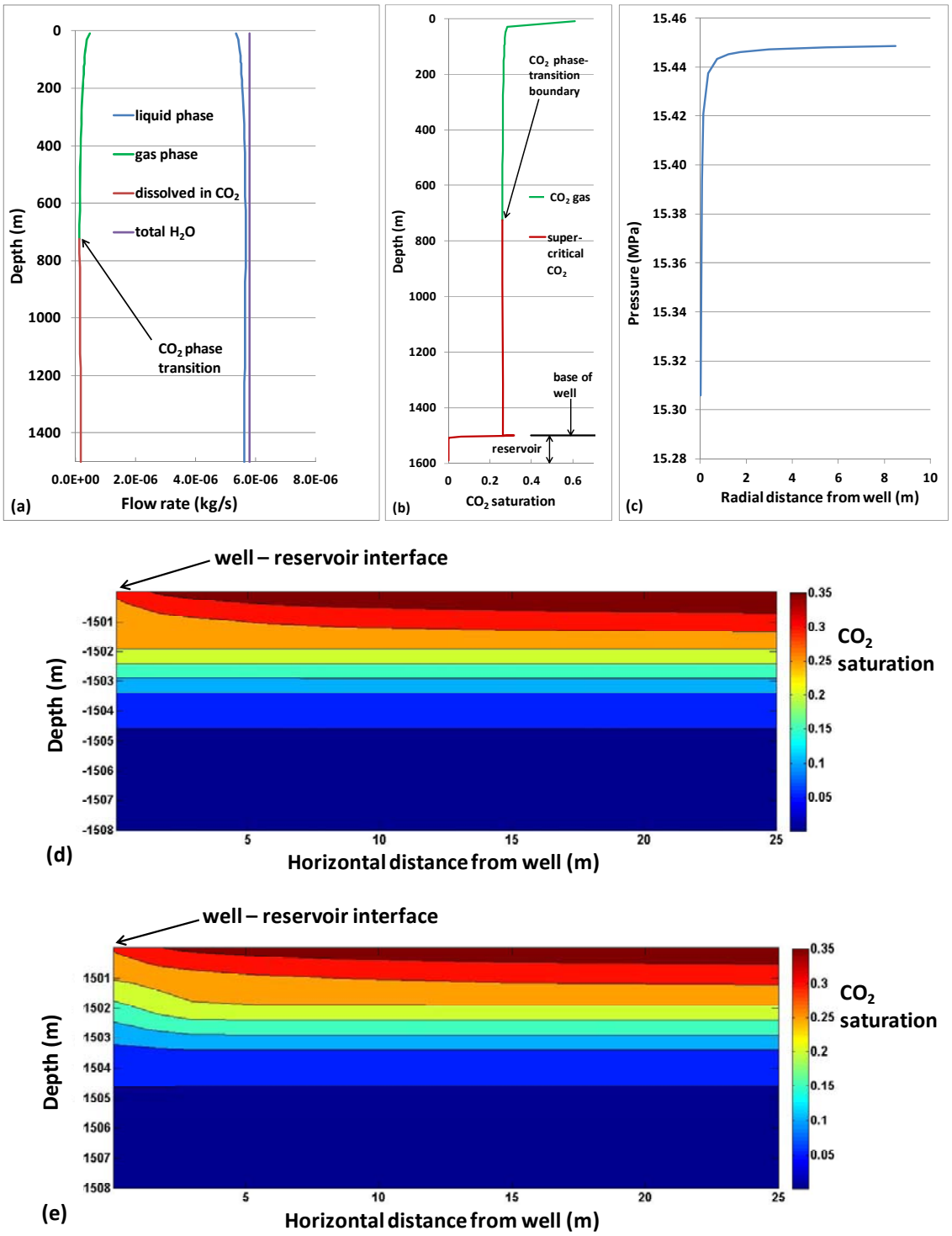
(a)
Depth (m)
Flow rate (kg/s)
liquid phase
gas phase
dissolved in CO2
total H2O
CO2 phase transition
(b)
Depth (m)
CO2 saturation
CO2 phase-transition boundary
CO2 gas
super-critical CO2
base of well
reservoir
(c)
Pressure (MPa)
Radial distance from well (m)
well – reservoir interface
(d)
Depth (m)
Horizontal distance from well (m)
CO2 saturation
well – reservoir interface
(e)
Depth (m)
Horizontal distance from well (m)
CO2 saturation

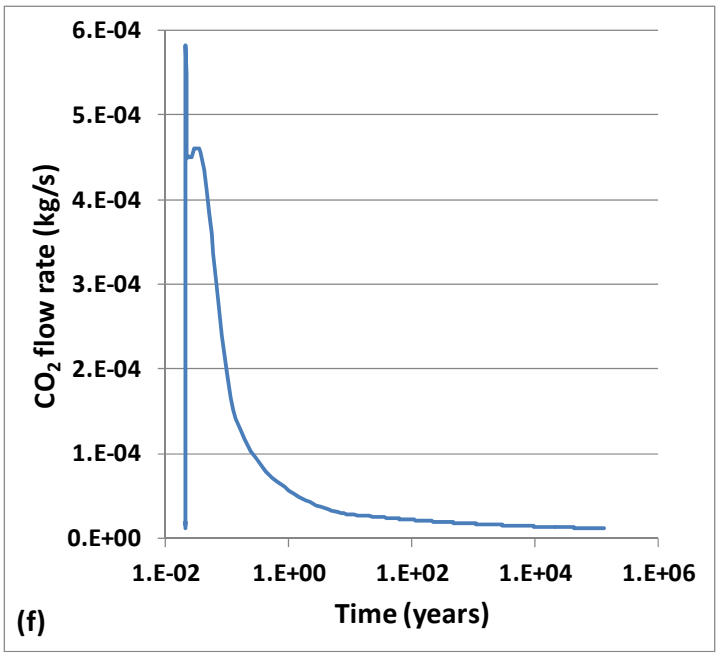

Figure 12: Results for leakage case rg31 (k_b = 1,000 darcy, k_r = 0.01 darcies, S_g = 0.01, R_{op} = 0.74 MPa). Strong thin-layer behavior. (a) H_2O mass flow rate at 1,000 years; (b) CO_2 phase saturation; (c) radial pressure profile along top of reservoir; (d) saturation contours at 1,000 years; (e) saturation contours at 256,000 years; (f) transient well leakage at ground surface.

4.5.3 Effect of Thick-Layer Versus Thin-Layer Behavior on Flow in the Borehole

Factors that control thick-layer versus thin-layer flow behavior are the CO_2 layer thickness (T), well permeability (k_b), reservoir permeability (k_r), and reservoir overpressure (R_{op}). These have been combined with factors of buoyancy pressure $(\Delta\rho gL)$and borehole radius (r_b) to make the following dimensionless group F_c:

$$F_c = \left(\frac{k_b}{k_r}\right)\left(\frac{2r_b}{T}\right)^3\left(\frac{\Delta\rho gL}{R_{op}}\right)^{0.5} \tag{19}$$

where $\Delta\rho$ is the supercritical CO_2-water density difference at the base of the well and L is the borehole depth. The most important aspect of thin-layer versus thick-layer behavior with respect to flow processes in the borehole is that thin-layer behavior can move brine up the borehole, whereas for thick-layer behavior, water present in the borehole does not contain dissolved salts. Simulations show that thin-layer behavior for some "borderline" cases with only weak flow of water up the borehole (rg16, rg46, and rg61, which all have k_b/k_r = 100,000) do not move sufficient quantities of salts from the storage reservoir to have much effect on the aqueous density in the borehole. The dimensionless group in Equation (19) is used to assess the density of the aqueous phase in the borehole, as shown in Figure 13. The curve fit is done by dividing the model data into two segments. For $F_c \leq 10$, density is a constant value, 1004 kg/m^3. As F_c rises above 10, the density rapidly rises to the maximum density represented by the aqueous density in the storage reservoir. The portion of the curve for $F_c > 10$ is given by

$$\rho_w = 1042.7[\log\{\log(F_c)\}]^{0.0028} \tag{20}$$

where ρ_w is the aqueous density in kg/m^3.

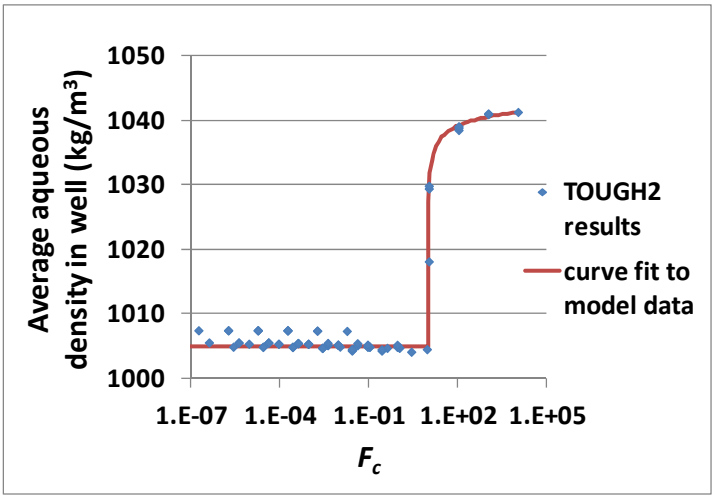

Figure 13: Average aqueous density in well versus dimensionless parameter, F_c.

The shale is assumed to be saturated with fresh water. Commonly, pore waters are expected to display increasing salinity with depth, but more complex salinity behaviors have been observed (Burst, 1976). For example, relatively fresh shale pore waters have been observed in association with more saline sandstone pore waters in Gulf Coast sediments (Schmidt, 1973). However, these more complex shale pore-water compositions were not investigated here. Fresh water in the shale has an average density of 995 kg/m^3, lower than the average aqueous density in the well, even for $F_c < 10$, cases where salts are not transported into the well. The effects of shale on well leakage are discussed further in the next section. The reason for the higher aqueous density in the well is that the average mass fraction of CO_2 for the aqueous phase in the well is much higher as compared with the shale, which has a negligible average mass fraction of CO_2. Although the fluid density of pure supercritical CO_2 is lower than pure water for conditions in the lower part of the well, water with dissolved CO_2 has a density greater than pure water. The upper end of the range (1007 kg/m^3) only occurs for the high overpressure cases, where the higher pressure increases the average CO_2 mass fraction for the aqueous phase in the well.

4.5.4 Effects of Shale Permeability on Well Leakage Flow Behavior

The cases discussed above all involve an essentially impermeable shale that caps the storage reservoir and surrounds the well (10^{-18} darcies). This impermeable condition was used not to represent typical shale conditions, but to reduce the number of factors influencing the leakage results. Some calculations were also performed using a more realistic shale permeability of 10^{-7} darcies. It was found that the shale permeability influenced the steady-state well-leakage rate in cases with well permeabilities of 100 darcies or lower, even though the shale permeability remains orders of magnitude lower than the well permeabilities. While CO_2 leakage into the shale is negligible compared with the CO_2 flow rate in the well, the higher shale permeability case allows water flow between the well and the shale. This resulted in a higher CO_2 saturation and hence higher CO_2 relative permeability in the well in the case with realistic shale permeability, as shown in Figure 14. This leads to a higher CO_2 leakage rate for the case with the realistic shale permeability. The case with higher CO_2 flow also has a higher water flow rate, but this can be attributed to the relatively low absolute value of the water flow rates that are predominantly carried as a dissolved phase in the CO_2 during flow up the well. The effect on

flow rates is dependent on well permeability, as shown in Figure 15. A number of additional calculations are needed to further investigate and understand this phenomenon, including the assumption in these calculations of a full contact area between flow in the well and the shale.

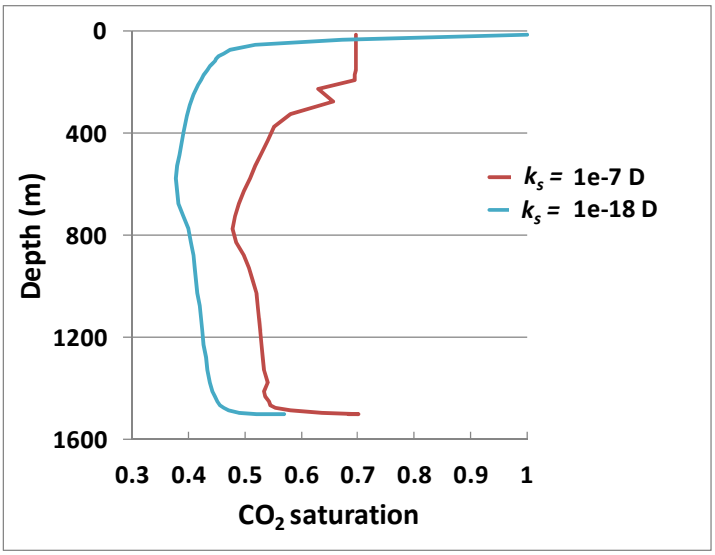

Figure 14: Water saturation profile for two cases of leaking wells that are the same except for the shale permeability (k_s). The low-permeability shale case is rg53; the higher shale permeability case is rg83. For both cases k_b = 1 darcy, k_r = 0.1 darcies, S_g = 0.5, R_{op} = 1.3 MPa. Note that "D" in the figures refers to the unit of permeability, "darcy."

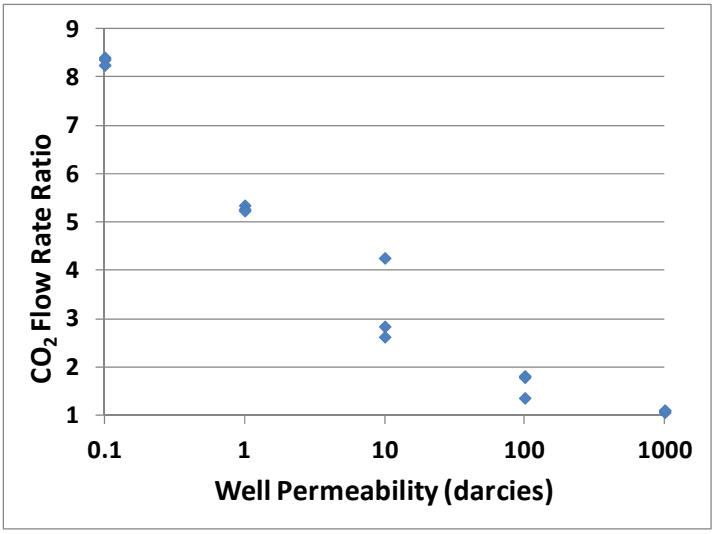

Figure 15: Ratio between well CO_2 flow rates for shale permeability of 10^{-7} darcy to that for shale permeability of 10^{-18} darcy, R_{op} = 1.2 MPa and average CO_2 saturation of 0.53 for both cases. The low-permeability shale cases are rg49-rg63; the higher shale permeability cases are rg79-rg93. Tables 2 and 3 present complete definitions of the different cases.

4.6 SIMULATION RESULTS FOR WELL-RESERVOIR COUPLING

In this section and later for the development of the PROM, flow conditions are assumed to be at steady state. However, steady-state conditions were not achieved for some of the cases

displaying thin-layer flow behavior. For these cases, well-leakage rates after 1,000 years of leakage were used as representative. One of the factors that stimulated this investigation, as outlined in Section 3, is the possibility that reservoir permeability may restrict well leakage through pressure draw-down in the reservoir caused by flow of fluids through the reservoir to the well. While this does occur, the flow behavior presented in Section 4.4 indicates that multiphase flow effects are more significant in terms of coupling between well-leakage and reservoir flow.

The results of these simulations regarding well-leakage and reservoir flow coupling for the group of simulations rg49–rg63 are shown in Figure 16. These simulations have an average reservoir saturation of 0.5, a CO_2-layer thickness of 80 m, and a reservoir overpressure of 1.3 MPa. Results for CO_2 leakage rates are shown in Figure 16(a), which are seen to be relatively insensitive to reservoir permeability, but strongly affected by well permeability. Figure 16(b) shows composite results for flow rate ratios against well-to-reservoir permeability ratios. Each well-rate ratio is the well flow rate for cases with reservoir permeability of 0.01 darcy and 0.1 darcy, divided by the well flow rate at identical saturation, overpressure, and well permeability conditions having a reservoir permeability of 1 darcy. The absence of a reservoir-interaction effect on well leakage gives a value of 1 for the CO_2 and water flow-rate ratios. These figures indicate that reservoir permeability has a relatively weak effect on well-leakage rates. Similar results are shown in Figures 16(c) and (d) for H_2O flow rates. CO_2 saturation and pressure at the base of the well are shown in Figures 16(e) and (f), respectively.

The variation in CO_2 saturation in the reservoir at the base of the well for cases having the same initial condition shows how leakage affects local reservoir saturations. For lower-permeability well conditions (0.1 and 1 darcy), CO_2 saturation is found to increase with increasing reservoir permeability. This behavior can be attributed to the relatively constant downward flow of water from the well into the reservoir for the same well permeability (as mentioned earlier, a result of exsolution of water as CO_2 moves up the well). A stronger tendency for water to collect at the base of the well for low-permeability reservoir conditions is seen in the saturation trends. Downward flow of water increases going from a well permeability of 0.1 to 1 darcy, because CO_2 flow rates are higher, leading to reduced saturations for the 1 darcy cases. The trend starts to deviate for the cases with well permeability of 10 darcies. For rg55 (k_b = 10 darcies, k_r =0.01 darcies), pressure drawdown jumps from 4500 Pa for rg52 (k_b = 1 darcies, k_r =0.01 darcies) to 20,000 Pa. This causes greater exsolution of water from CO_2 prior to entering the well, leaving less water available in the CO_2 for release into the well. The result is that the downward water flow rate for rg55 is similar to that in rg52, and CO_2 saturations are likewise similar. The same pressure drawdown effect leading to reduced downward water flow in the well occurs for rg58 (k_b = 100 darcies, k_r =0.01 darcies) and rg59 (k_b = 100 darcies, k_r =0.1 darcies), boosting CO_2 saturations; the downward flow rate for rg59 is about a factor of ten lower than for rg60 (k_b = 100 darcies, k_r =1 darcies), but this is mirrored by the differences in reservoir permeabilities, resulting in similar CO_2 saturations for these cases. Increased pressure depletion affects rg61 (k_b = 1,000 darcies, k_r =0.01 darcies), 712,000 Pa; rg62 (k_b = 1,000 darcies, k_r =0.1 darcies), 104,000 Pa; and rg63 (k_b = 100 darcies, k_r =0.1 darcies), 19,000 Pa. However, the trend again changes because pressure depletion also begins to change the entire reservoir saturation profile in a coning flow pattern, which tends to lower CO_2 saturations near the base of the well. The counteracting effects of coning and reduced water flow down the well (for case rg61, water flow is upward throughout the well) lead to the saturation patterns observed.

In Figure 16(f), pressure depletion is clearly seen to be strongest for the highest well permeability (1,000 darcies)/lowest reservoir permeability (0.01 darcies) case, rg61, which corresponds to the permeability ratio (10^5) found in Section 3, where pressure depletion starts to have an impact on well leakage for single-phase flow. This is also the only case in this group to display thin-layer behavior (see Section 4.4).

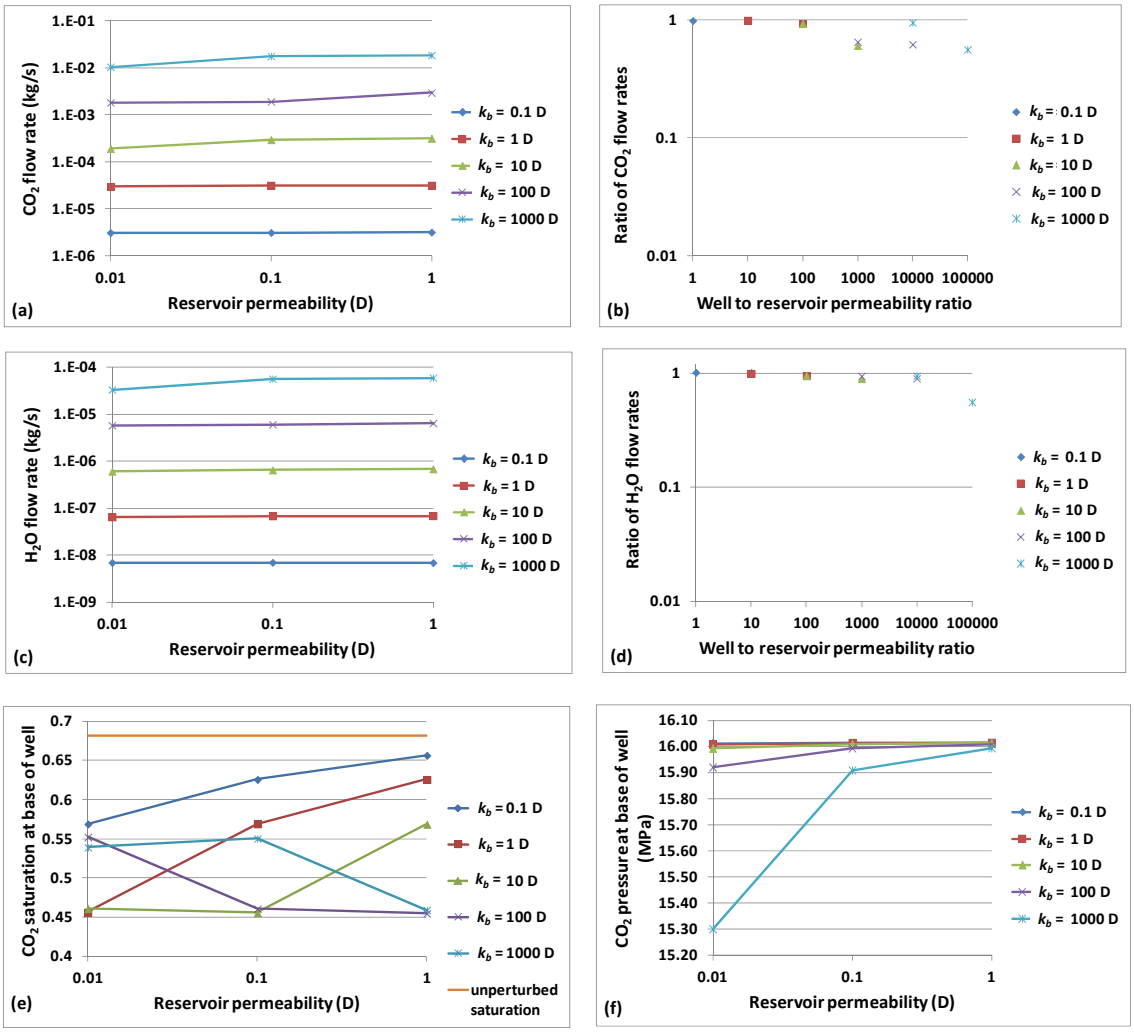

Figure 16: CO_2 and H_2O flow rates and CO_2 saturations and pressures at the base of the well for different combinations of reservoir and well permeabilities (k_b), cases rg49-rg63; S_g = 0.5, R_{op} = 1.3 MPa. (a) CO_2 mass flow rates at ground surface; (b) Ratio of maximum CO_2 mass flow rate to other CO_2 mass flow rates at the same well permeability but different reservoir permeabilities; (c) H_2O flow rates at ground surface; (d) Ratio of maximum H_2O mass flow rate to other H_2O mass flow rates at the same well permeability but different reservoir permeabilities; (e) CO_2 saturation in reservoir at base of well; (f) CO_2 pressure in reservoir at base of well. Note that "D" in the figures refers to the unit of permeability, "darcy."

Results of simulations having high overpressure, rg64–rg75, are given in Figure 17. These simulations have an average reservoir saturation of 0.5, a CO_2 layer thickness of 80 m and a reservoir overpressure of 5.2 MPa. Results for CO_2 leakage rates are shown in Figure 17(a), which are similar to those in Figure 16(a). Figure 17(b) shows composite results for flow-rate ratios against well-to-reservoir-permeability ratios. These results indicate that reservoir permeability has a relatively weak effect on well-leakage rates. Similar results are shown in

Figures 17(c) and (d) for H_2O flow rates. CO_2 saturation and pressure at the base of the well are shown in Figures 17(e) and (f), respectively. Similar trends are seen for saturation in Figure 17(e) as found in Figure 16(e). Pressure depletion is clearly seen to be strongest for the highest well-permeability (1,000 darcies)/lowest reservoir-permeability (0.01 darcies) case, rg73. None of these cases show thin-layer behavior; however, note that the 1,000-darcy well results are not available because of instability in the numerical solution for these cases.

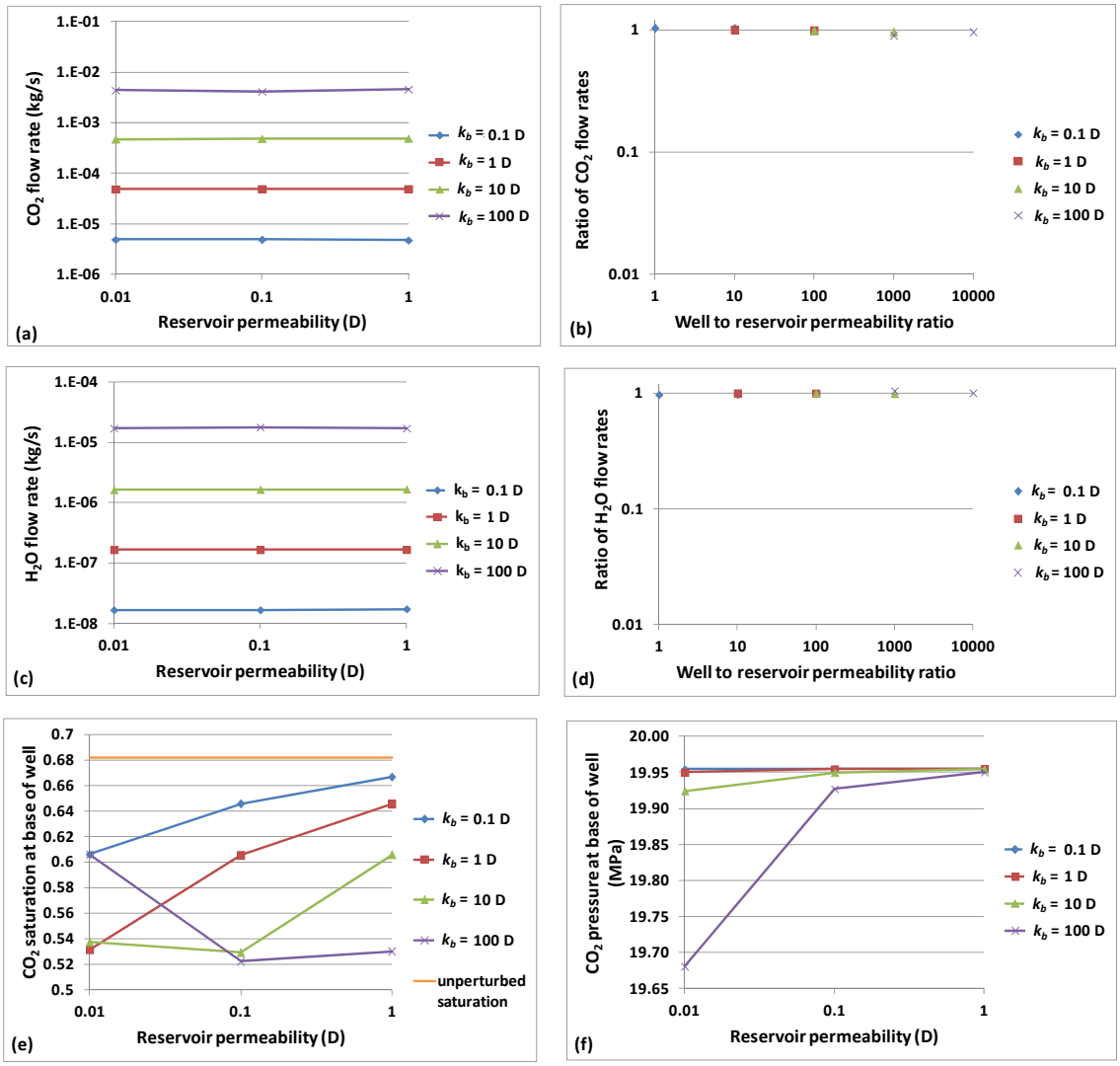

Figure 17: CO_2 and H_2O flow rates and CO_2 saturations and pressures at the base of the well for different combinations of reservoir and well permeabilities (k_b), cases rg64-rg75; S_g = 0.5, R_{op} = 5.2 MPa. (a) CO_2 mass flow rates at ground surface; (b) Ratio of maximum CO_2 mass flow rate to other CO_2 mass flow rates at the same well permeability but different reservoir permeabilities; (c) H_2O flow rates at ground surface; (d) Ratio of maximum H_2O mass flow rate to other H_2O mass flow rates at the same well permeability but different reservoir permeabilities; (e) CO_2 saturation in reservoir at base of well; (f) CO_2 pressure in reservoir at base of well. Note that "D" in the figures refers to the unit of permeability, "darcy."

Results of simulations having low overpressure, rg4–rg18, are given in Figure 18. These simulations have an average reservoir saturation of 0.5, a CO_2-layer thickness of 80 m, and a reservoir overpressure of 0.03 MPa. Results for CO_2 leakage rates are shown in Figure 18(a),

which are similar to those in Figure 16(a). Figure 18(b) shows composite results for flow-rate ratios against well-to-reservoir permeability ratios. These results indicate that reservoir permeability has a relatively weak effect on well-leakage rates. Similar results are shown in Figures 18(c) and (d) for H_2O flow rates. CO_2 saturation and pressure at the base of the well are shown in Figures 18(e) and (f), respectively. Similar trends are seen for saturation in Figure 18(e) as found in Figure 16(e). Pressure depletion is clearly seen to be strongest for the highest well-permeability (1,000 darcies)/lowest reservoir-permeability (0.01 darcies) case, rg16. This is also the only case in this group to display thin-layer behavior (see Section 4.4).

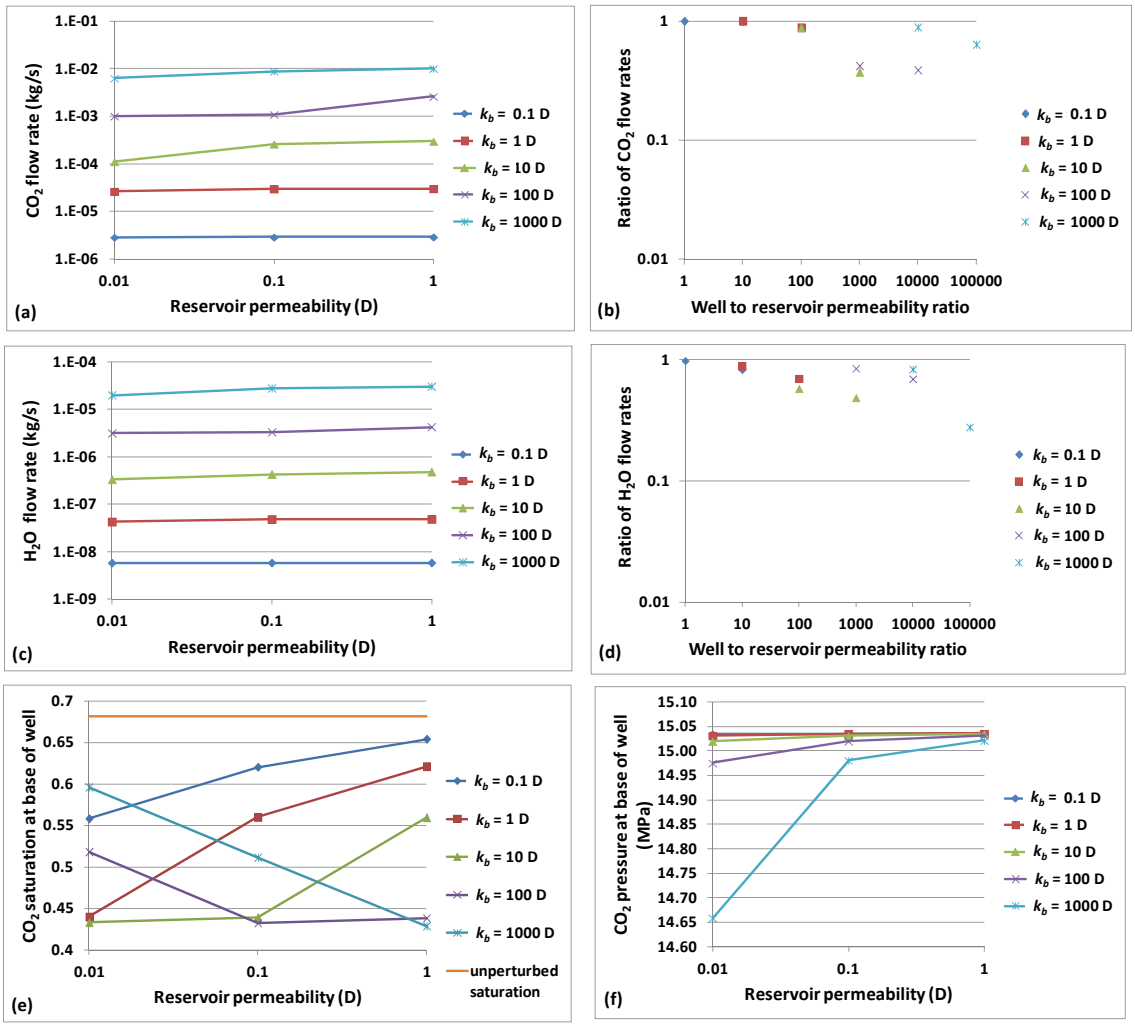

Figure 18: CO_2 and H_2O flow rates and CO_2 saturations and pressures at the base of the well for different combinations of reservoir and well permeabilities (k_b), cases rg4-rg18; S_g = 0.5, R_{op} = 0.03 MPa. (a) CO_2 mass flow rates at ground surface; (b) Ratio of maximum CO_2 mass flow rate to other CO_2 mass flow rates at the same well permeability but different reservoir permeabilities; (c) H_2O flow rates at ground surface; (d) Ratio of maximum H_2O mass flow rate to other H_2O mass flow rates at the same well permeability but different reservoir permeabilities; (e) CO_2 saturation in reservoir at base of well; (f) CO_2 pressure in reservoir at base of well. Note that "D" in the figures refers to the unit of permeability, "darcy."

Results of simulations having a reduced CO_2 layer thickness, rg34–rg48, are given in Figure 19. These simulations have an average reservoir saturation of 0.2, a CO_2-layer thickness of 20 m and a reservoir overpressure of 0.99 MPa. Results for CO_2 leakage rates are shown in Figure 19(a),

which are similar to those in Figure 16(a). Figure 19(b) shows composite results for flow-rate ratios against well to reservoir permeability ratios. These results indicate that reservoir permeability has a relatively weak effect on well-leakage rates. Similar results are shown in Figures 19(c) and (d) for H_2O flow rates. CO_2 saturation and pressure at the base of the well are shown in Figures 19(e) and (f), respectively. Similar trends are seen for saturation in Figure 19(e) as found in Figure 16(e). Pressure depletion is clearly seen to be strongest for the highest well-permeability (1,000 darcies)/lowest reservoir-permeability (0.01 darcies) case, rg46. This is also the only case in this group to display thin-layer behavior (see Section 4.4).

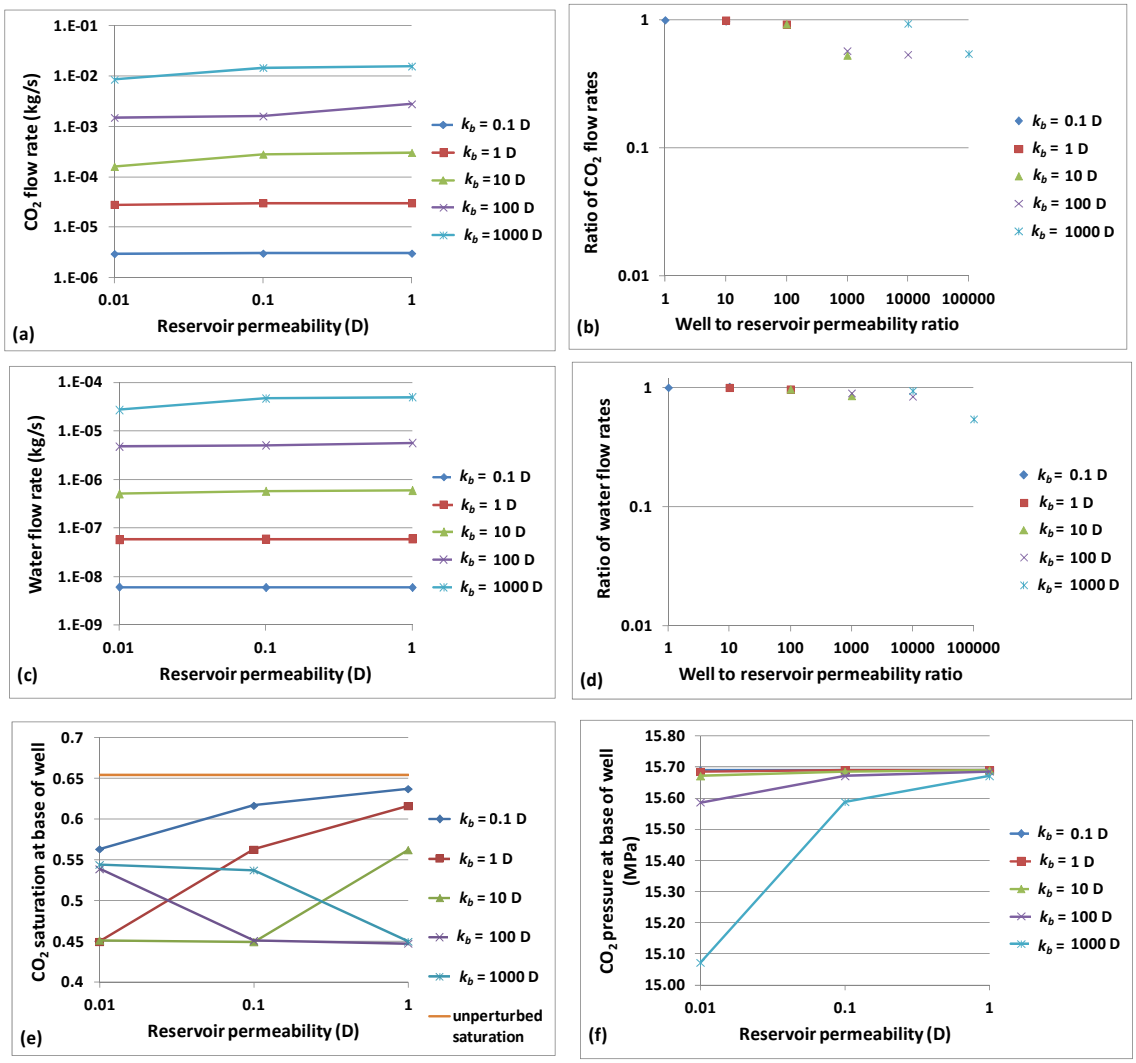

Figure 19: CO_2 and H_2O flow rates and CO_2 saturations and pressures at the base of the well for different combinations of reservoir and well permeabilities (k_b), cases rg34-rg48; S_g = 0.2, R_{op} = 0.99 MPa. (a) CO_2 mass flow rates at ground surface; (b) Ratio of maximum CO_2 mass flow rate to other CO_2 mass flow rates at the same well permeability but different reservoir permeabilities; (c) H_2O flow rates at ground surface; (d) Ratio of maximum H_2O mass flow rate to other H_2O mass flow rates at the same well permeability but different reservoir permeabilities; (e) CO_2 saturation in reservoir at base of well; (f) CO_2 pressure in reservoir at base of well. Note that "D" in the figures refers to the unit of permeability, "darcy."

Results of simulations having the thinnest CO_2 layer thickness in the storage reservoir, rg19-rg33, are given in Figure 20. These simulations have an average reservoir saturation of 0.01, a

CO_2 layer thickness of 3 m, and a reservoir overpressure of 0.74 MPa. Results for CO_2 leakage rates are shown in Figure 20(a), which shows some different trends from those found in the other groups Figures 16(a) through 19(a). Figure 20(b) shows composite results for flow rate ratios against well-to-reservoir permeability ratios. Of the 15 cases in this group, nine cases (rg22, rg25, rg26, and rg 28-33) have a thin-layer response, i.e., no downward water flow in the well. At low well permeabilities (0.1 and 1 darcy), thick-layer behavior is found, and the trends in CO_2 flow rate with reservoir permeability are similar to those found in the other groups. However, for thin-layer behavior, well-leakage rates are more significantly coupled to reservoir flow behavior. Coning-type flow is associated with a thin-layer response and is mainly responsible for the differing leakage trends found for this group. The coning flow response is stronger for higher well permeability and lower reservoir permeability, reinforcing reservoir-permeability effects and depressing CO_2 flow rates at lower reservoir permeabilities. The result is an increasing CO_2 flow rate for cases with the same well permeability and increasing reservoir permeability. By contrast, H_2O flow rates remain relatively unaffected by the reservoir permeability, as shown in Figures 20(c) and 20(d). At low well permeabilities, H_2O flow rates are determined mainly by the CO_2 flow rate and associated dissolved H_2O. At high well permeabilities, the aqueous phase enters the well directly. However, the coning effect in the reservoir, which is stronger for low reservoir permeabilities, increases water saturations near the well and tends to offset the effects of reduced reservoir permeabilities on H_2O flow rates into the well. CO_2 saturation and pressure at the base of the well are shown in Figures 20(e) and (f), respectively. CO_2 saturation trends at low to moderate well permeabilities are similar to those found for the other groups. However, coning depresses CO_2 saturation at the highest well permeabilities (100 and 1,000 darcies), particularly for high well-to-reservoir permeability ratios. Pressure depletion is clearly seen to be strongest for the highest well-permeability (1,000 darcies)/lowest reservoir-permeability (0.01 darcies) case, rg31.

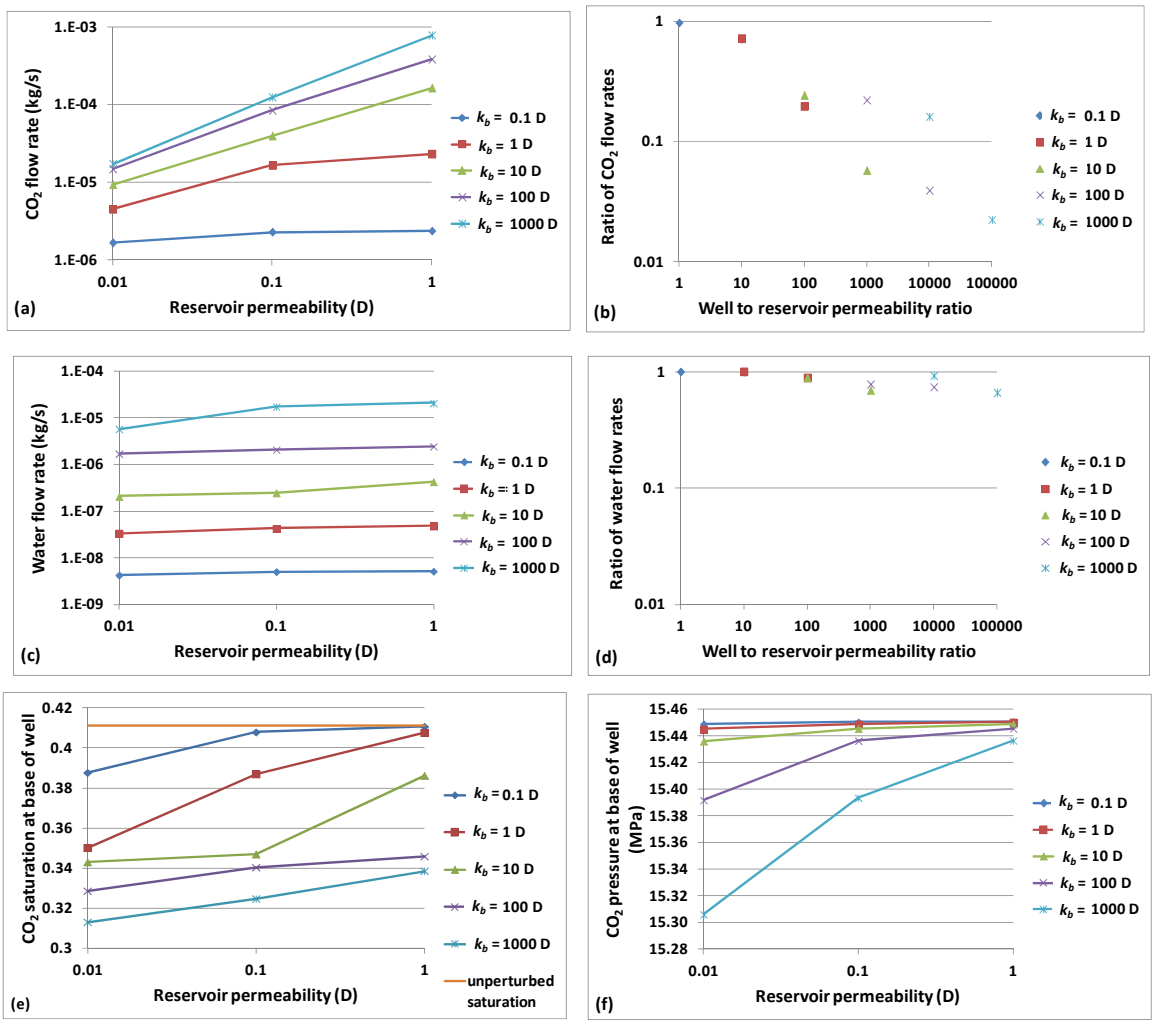

Figure 20: CO_2 and H_2O flow rates and CO_2 saturations and pressures at the base of the well for different combinations of reservoir and well permeabilities (k_b), cases rg19-rg33; S_g = 0.01, R_{op} = 0.74 MPa. (a) CO_2 mass flow rates at ground surface; (b) Ratio of maximum CO_2 mass flow rate to other CO_2 mass flow rates at the same well permeability but different reservoir permeabilities; (c) H_2O flow rates at ground surface; (d) Ratio of maximum H_2O mass flow rate to other H_2O mass flow rates at the same well permeability but different reservoir permeabilities; (e) CO_2 saturation in reservoir at base of well; (f) CO_2 pressure in reservoir at base of well. Note that "D" in the figures refers to the unit of permeability, "darcy."

4.7 SIMULATION RESULTS FOR WELL SATURATION

The development of a reduced-order model for well leakage requires the specification of saturation conditions for the leakage process. Previous well-leakage analyses performed by Jordan and Stauffer (2011) for development of reduced-order models for well leakage used a decoupled well, in which saturation, pressure, and temperature were specified at the base of the well (see Appendix). The simulations conducted here provide the relationship between saturations at the well in the absence of well leakage and in the presence of well leakage when the well is coupled to the reservoir. Only three initial saturation conditions in the reservoir were used for these simulations; the resulting saturations in the reservoir cell immediately below the well are given in Figure 21.

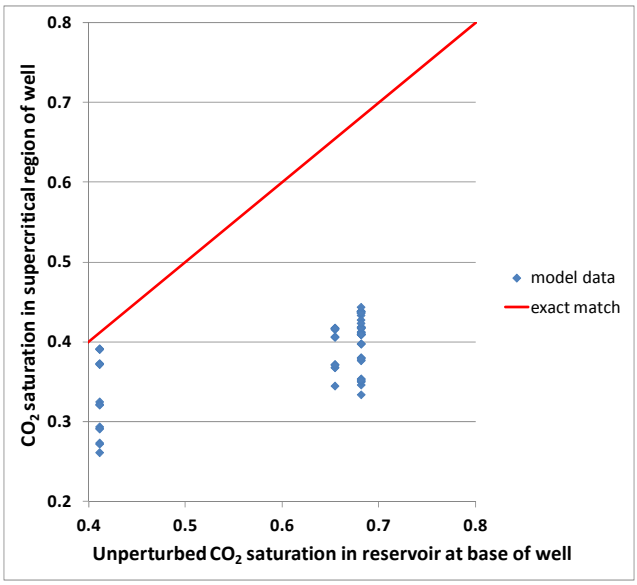

Figure 21: Unperturbed CO_2 saturations in the reservoir at the base of the well versus average CO_2 saturation in the supercritical region in the well.

As can be seen from Figure 21, the correlation between unperturbed CO_2 saturations in the reservoir immediately below the well and average CO_2 saturations in the supercritical region of the well is not strong. Furthermore, the figure also shows large differences between reservoir saturations at the base of the well and saturations in the well, especially for the high-reservoir saturation cases. As discussed in Section 5.1, CO_2 saturations in the well are also strongly affected by factors of well permeability, reservoir permeability, and reservoir overpressure, leading to the weak relationship shown here with the unperturbed CO_2 saturation in the reservoir immediately below the well.

4.8 SIMULATION RESULTS FOR WELL TEMPERATURE

Temperature profiles for some cases are given in Figure 22. The initial temperature follows a linear profile from 15–60°C between the top and base of the well. There is not a great deal of change in temperature for most cases as a result of well leakage. CO_2 leakage rates range from 2×10^{-6} to 0.02 kg/s. Case rg63 shows some cooling in the region just above the phase transition and has one of the highest CO_2 flow rates investigated.

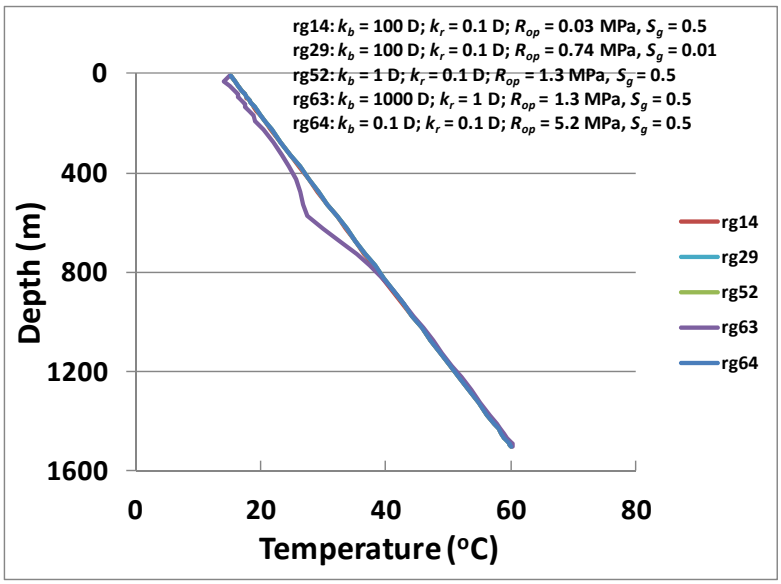

Figure 22: Temperature profiles in well. Note that "D" in the figures refers to the unit of permeability, "darcy" for well permeability (k_b) and reservoir permeability (k_r), R_{op} is the reservoir overpressure, and S_g is the average CO_2 saturation in the reservoir (see Table 2).

5. PHYSICS-BASED REDUCED-ORDER MODELS

PROMs were developed for well leakage in the case of simultaneous, steady CO_2 and water flow through a well from the reservoir to the surface. A PROM is a type of reduced-order model that utilizes some level of physics-based computation, in this case for well leakage, which is used directly in the risk assessment. This may be distinguished from other reduced-order models that typically use a physics-based model to compute a response surface used in the risk assessment. The PROM developed here utilizes a simplified mathematical model that can be implemented using closed-form analytical mathematical forms in an attempt to capture some of the major dependencies for well leakage on known independent variables. This helps to stabilize the PROMs, because at least some of the intrinsic variability of the system response is based on theoretical mathematical relationships used by detailed process simulators such as TOUGH2-ECO2M. Because the mathematical model is simplified, however, it will not be able to exactly reproduce all results from a numerical simulator, and generally requires calibration.

The starting point for a PROM for CO_2 leakage is based on Darcy's equation for two-phase flow:

$$\dot{m}_g = -\frac{Ak_b k_{rg}}{\nu_g}\left(\frac{dp}{dz} + \rho_g g\right), \tag{21}$$

where $\dot{m}_g$ is the mass flow rate of CO_2 in the well, k_b is the permeability of the well, k_{rg} is the relative permeability to CO_2, ν_g is the kinematic viscosity of CO_2, A is the cross-sectional area of the well, p is the fluid pressure, ρ_g is the density of CO_2, g is the gravitational acceleration, and z is the vertical coordinate (positive upwards). For steady-flow conditions, $\dot{m}_g$ is constant for all depths in the well. If well leakage does not impact conditions in the reservoir too strongly, most of the quantities in the Darcy equation are known at the bottom of the well from an uncoupled reservoir simulation. Therefore, the mass flow rate is computed at that location. The relative permeability to CO_2 at the bottom of the well is a function of CO_2 saturation. However, CO_2 saturation in the well is not given directly by unperturbed saturation conditions in the reservoir , as discussed in Section 4.7. Viscosity and density of CO_2 are obtained from known temperature and pressure conditions at the bottom of the well, using equation-of-state relationships. Other aspects that characterize the well— A, k_b, and well depth— are known. The pressure gradient, $\frac{dp}{dz}$, is not known, but is approximated by the pressure difference between the ground surface and the bottom of the well, divided by the depth of the well. Note that the phase pressure difference between CO_2 and water is not considered, i.e., capillary pressure is approximated as zero. Also, this model does not include leak-off of fluids from the well to intermediate thief zones.

Similarly for H_2O leakage, the Darcy equation is used:

$$\dot{m}_w = -\frac{Ak_b k_{rw}}{\nu_w}\left(\frac{dp}{dz} + \rho_w g\right). \tag{22}$$

An example of the use of PROMs based on the Equations (21) and (22) and calibrated with uncoupled well-leakage process-model results is given in the Appendix.

Slight extensions of the Darcy expressions given in Equations (21) and (22) are used here for the calibration to the coupled reservoir-well process model results:

$$\dot{m}_g = -\frac{Ak_b k_{rg}\beta_g}{\nu_g}\left(\frac{dp}{dz} + \rho_g g\right) \tag{23}$$

$$\dot{m}_w = -\frac{Ak_b k_{rw}\beta_w}{\nu_w}\left(\frac{dp}{dz} + \rho_w g\right) + \beta_w \dot{m}_g X, \tag{24}$$

The additional term in the mass flow rate for water accounts for the transport of water dissolved in CO_2, where X is the mass fraction of H_2O in CO_2. This assumes that the CO_2 mass flow rate associated with CO_2 dissolved in water is negligible, which was true for the cases investigated here. The water mole fraction in CO_2 is ~0.01 at conditions of 15 MPa and 60°C (Sabirzyanov et al., 2002), resulting in a mass fraction of 0.004. This turns out to be important for the low-rate water mass flow rates as compared with CO_2 mass flow rates found in these simulations. In addition, fitting coefficients have been added as scaling factors for the overall flow rates. The fitting coefficients are potentially needed to correct for the saturation, phase properties, and pressure gradient at the base of the well, which are not known without more detailed simulations such as those presented in Section 4. These changes were found to provide a better match with the coupled reservoir-well model results. In this case, the extended van Genuchten relative permeability functions, Equations (16) through (18), are used, as also used in the process model.

5.1 UNCALIBRATED RESULTS AND CALIBRATION DIRECTLY USING FITTING COEFFICIENTS

The first PROM shown in Figure 23 uses the reservoir saturations at the base of the well unperturbed by well leakage without calibration of the β_g and β_w fitting coefficients in Equations (23) and (24). The results show some correlation, but the mean-square relative errors are large. In adjusting the β_g and β_w fitting coefficients, we significantly improve the mean-square relative error, as shown in Figure 24. Scatter for the low-saturation cases appears to dominate the error for the CO_2 flow rate whereas for H_2O, deviations at higher flow rates dominate the error. For most of the cases, H_2O flow rates in the well are determined by the amount of H_2O entering the well dissolved in the CO_2. Therefore, the β_g fitting coefficient influences both the CO_2 and H_2O flow rates. This shows that fitting coefficients significantly different than 1 are needed when using Equations (23) and (24), without providing more detailed information about phase saturations and phase properties in the well.

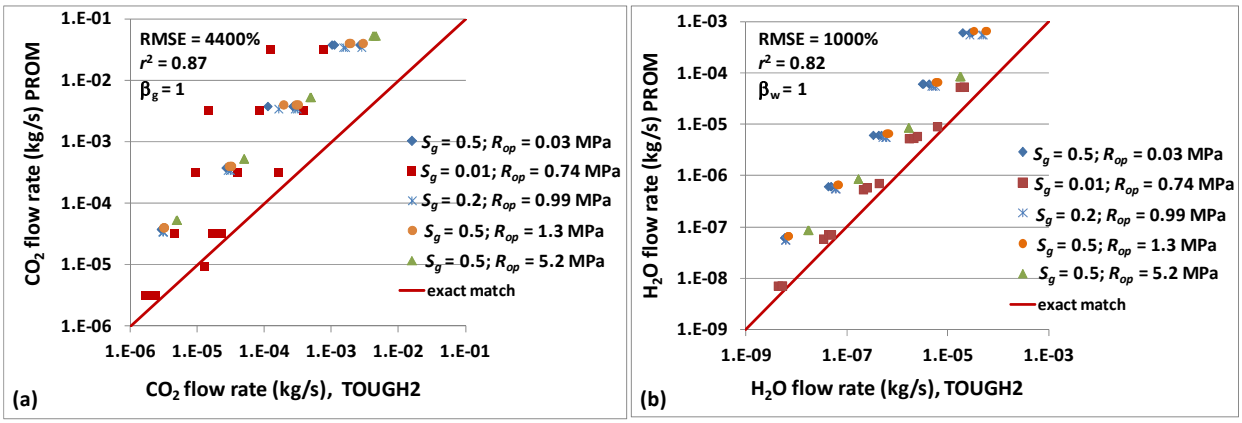

Figure 23: Uncalibrated PROMs that use unperturbed reservoir saturations for the well. (a) CO_2 flow rate PROM comparison; (b) H_2O flow rate PROM comparison. RMSE is the root-mean-square relative error, and r is the sample Pearson correlation coefficient. β_g and β_w are calibration parameters defined in Equations (23) and (24), but are uncalibrated here. S_g is the average CO_2 saturation in the storage reservoir, and R_{op} is the reservoir overpressure.

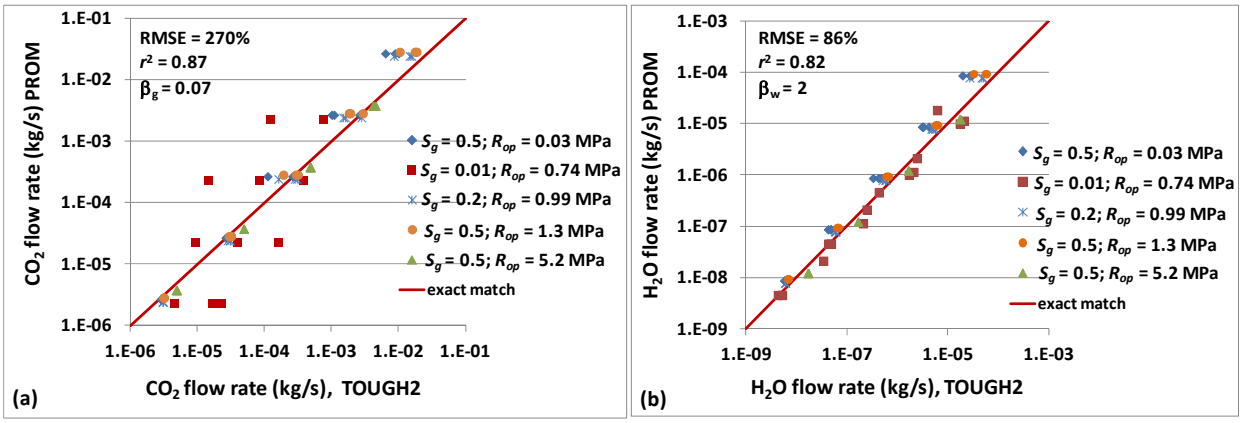

Figure 24: Calibrated PROMs that use unperturbed reservoir saturations for the well. (a) CO_2 flow rate PROM comparison; (b) H_2O flow rate PROM comparison. RMSE is the root-mean-square relative error, and r is the sample Pearson correlation coefficient. β_g and β_w are calibrated parameters defined in Equations (23) and (24). S_g is the average CO_2 saturation in the storage reservoir, and R_{op} is the reservoir overpressure.

5.2 CALIBRATION USING CORRELATIONS FOR SATURATION AND AQUEOUS DENSITY IN THE WELL

As discussed previously, the reservoir saturations at the base of the well do not, in many cases, provide good estimates of saturations in the well during leakage (Figure 21). Saturations in the well during well leakage are correlated with well permeability, reservoir permeability, and overpressure, in addition to the saturation in the reservoir. Average water saturation in the lower part of the well where CO_2 is supercritical was found to produce good results when used for the relative permeability functions implemented in these PROMs. However, the PROMs cannot directly use information from the process model concerning conditions in the well, or else a process model needs to be run for each case. Therefore, a linear regression between average CO_2 saturation in the well (S_{gb}) within the supercritical CO_2 region was generated as a function of

the log of the well permeability, $\log(k_b)$, the log of the unperturbed CO_2 saturation in the reservoir at the base of the well, $\log(S_{gr})$, reservoir overpressure, R_{op}, log of the reservoir permeability, $\log(k_r)$, and all products of these factors:

$$\begin{aligned} S_{gb} = {} & a_0 + a_1\log(k_b) + a_2\log(S_{gr}) + a_3 R_{op} + a_4\log(k_r) + a_5\log(k_b)\log(S_{gr}) \\ & + a_6\log(k_b)R_{op} + a_7\log(k_b)\log(k_r) + a_8\log(S_{gr})R_{op} \\ & + a_9\log(S_{gr})\log(k_r) + a_{10}R_{op}\log(k_r) + a_{11}\log(k_b)\log(S_{gr})R_{op} \\ & + a_{12}\log(k_b)R_{op}\log(k_r) + a_{13}\log(k_b)\log(S_{gr})\log(k_r) \\ & + a_{14}\log(S_{gr})R_{op}\log(k_r) + a_{15}\log(k_b)\log(S_{gr})R_{op}\log(k_r) \end{aligned} \tag{25}$$

where a_0 =0.6312, a_1 =-0.2871, a_2 =1.3339, a_3 =-0.2442, a_4 =-0.2448, a_5 =-1.7000, a_6 =0.4057, a_7 =-0.09368, a_8 =-1.5009, a_9 =-1.5272, a_{10} =0.3381, a_{11} =2.4305, a_{12} =0.1412, a_{13} =-0.6095, a_{14} =2.0385, a_{15} =0.8542.

The correlation was developed first through linear regression of 30 points shown in Figure 25(a). The remaining 42 points are used for validation by comparing the actual simulated values and predicted values using Equation (25), as shown in Figure 25(b).

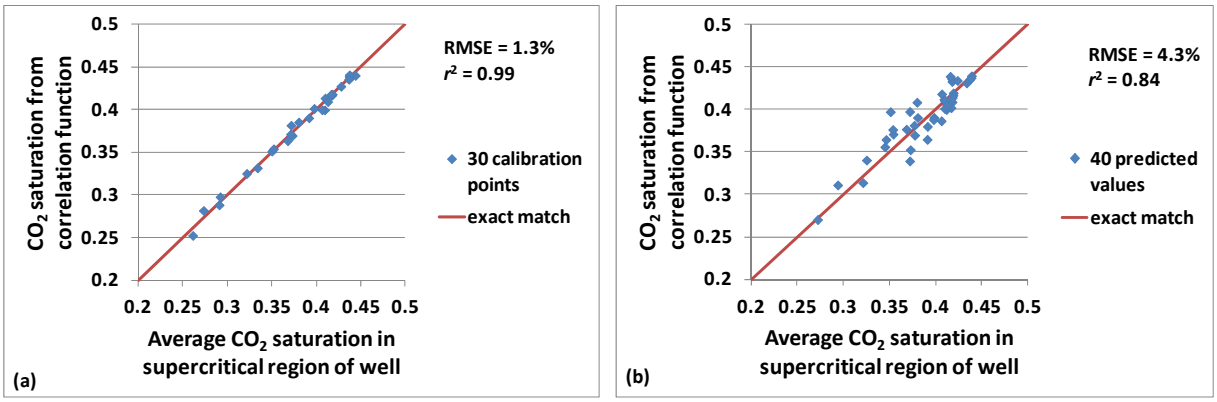

Figure 25: Correlation between Average Water Saturation in Supercritical Region of Well with Well Permeability, Reservoir Overpressure, and Reservoir Permeability. (a) calibration points; (b) predicted values. RMSE is the root-mean-square relative error and *r* is the sample Pearson correlation coefficient.

Using Equation (25) as a predictor for saturation used in the relative permeability functions in the PROMs, along with Equation (20) for aqueous density, does substantially improve the results, as shown in Figure 26. Notably for this calibration, β_g and β_w have values of 1. The two points at high H_2O flow rates that deviate from the group are influenced by pressure drawdown in the reservoir, an effect that is not included in the PROMs. Both of these cases, rg46 and rg61, have well-to-reservoir permeability ratios of 10^5, the highest included in this study. The impact of pressure drawdown can be greater for H_2O flow rates, because pressure is the only driving force for moving a bulk aqueous phase up the well, unlike CO_2, which is also affected by buoyancy forces.

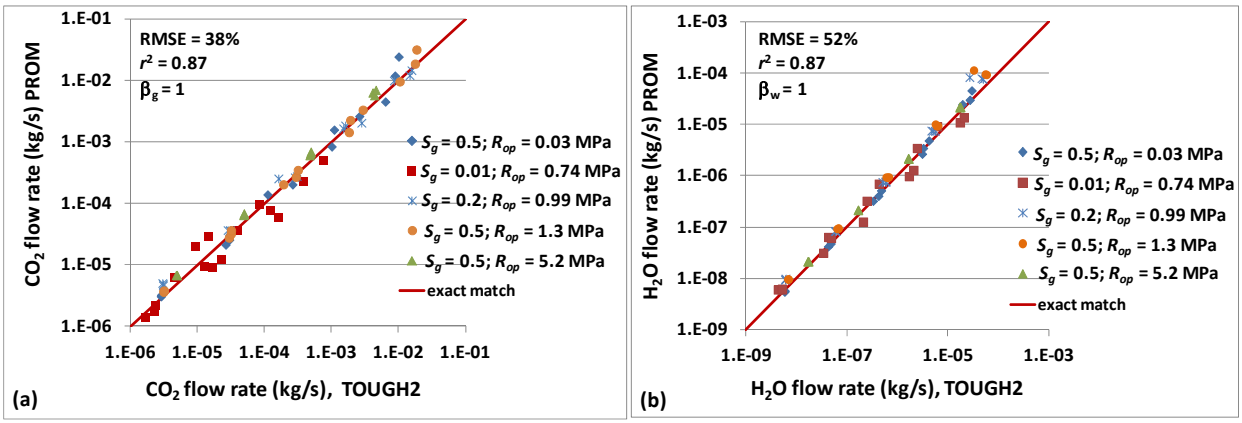

Figure 26: PROMs that use a saturation correlation function and aqueous density correlation function. (a) CO_2 flow rate PROM comparison; (b) H_2O flow rate PROM comparison. RMSE is the root-mean-square relative error, and r is the sample Pearson correlation coefficient. β_g and β_w are fitting parameters defined in Equations (23) and (24), but are not calibrated in these PROMs. S_g is the average CO_2 saturation in the storage reservoir, and R_{op} is the reservoir overpressure.

6. DISCUSSION OF ALTERNATIVE PROMS

The process-model flow simulations discussed in Section 4 and the steady-state PROMs presented in Section 5 suggest a number of different ways that PROMs may be developed to address the identified features of well leakage and coupling with reservoir flow. A potentially feasible and more accurate approach than the PROMs given in Section 5 would be to directly use a simulator similar to the one used in Section 4 in the risk assessment, shown schematically in Figure 27 (a). This simulator can include transient conditions as well as all the processes identified as important in this study, including all flow effects in the reservoir and flow interactions with shale. The advantages to this simulator are that it gives a direct representation of physical processes and more flexibility to add additional processes into the well-leakage PROM. Although it would increase computational effort significantly in the actual scenario with many leaky wells, multiple well-leakage simulations are easily parallelizable.

A simplification that may not sacrifice too much of the flow physics would be to reduce the numerical simulator to a pseudo-one-dimensional version of the full model, shown in Figure 27(b). In this PROM, the effect of multi-dimensional flow in the reservoir and interactions with shale would need to be simplified to a one-dimensional problem. For example, in the reservoir, flow to the well could be approximated as a one-dimensional spherical or cylindrical flow system, with geometrical factors based on spherical and/or cylindrical geometry. The interactions with shale can be treated by a semianalytical solution in a similar manner as Pruess (2011b). This approach still retains direct representation of multi-phase, multi-component effects that have been found to be important.

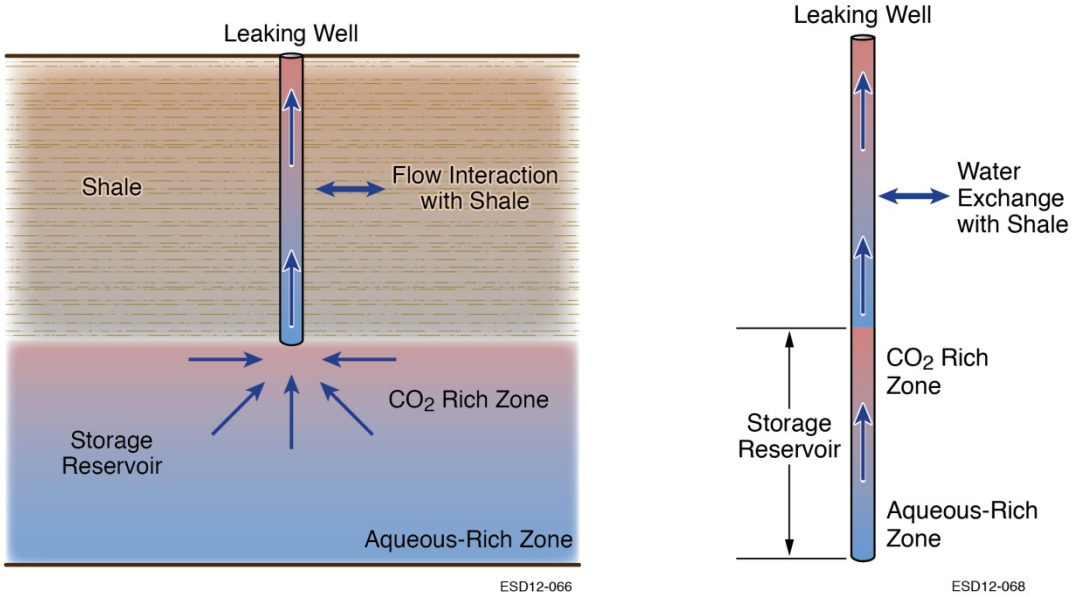

Figure 27: Multi-phase, multi-component PROMs using a numerical simulation approach: (a) a multi-dimensional model; (b) a psudo-one-dimensional model with spherical or cylindrical flow geometry in storage reservoir and simple exchange model with shale.

Taking a another step down in complexity, the PROMs developed in Section 5 could be used directly with some adjustments to conservatively bound transient flow and shale interaction effects, or could be expanded in an attempt to include these through more complex analytical

models or additional correlations developed from numerical process-model results (Figure 28(a)). Multi-phase, multi-component flow effects are included indirectly in these PROMs through correlations developed from process-model results. The least complex analytical PROM, such as given in the Appendix, could be linked directly to uncoupled reservoir simulation information from the reservoir risk assessment model, as shown in Figure 28(b). However, for some cases, such an approach may require substantial conservatism in the leakage estimates. These simpler analytical approaches are much faster and more stable computationally than the numerical methods, but miss some of the physics of the problem and, therefore, will be less accurate than the numerical methods.

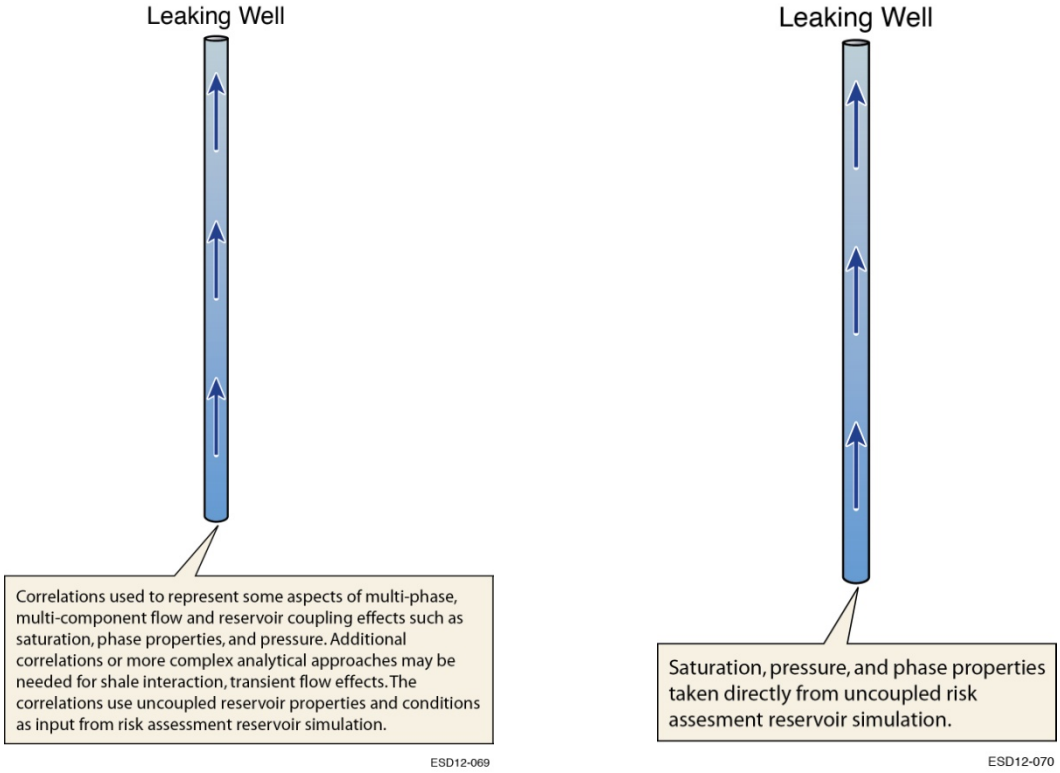

Figure 28: Analytical PROMs: (a) supported by correlations for process complexities not directly represented; (b) simple analytical PROM using uncoupled reservoir model inputs.

7. SUMMARY AND CONCLUSIONS

Coupled well leakage with reservoir flow effects were investigated using TOUGH2-ECO2M, a numerical model that accounts for multi-phase flow, heat transfer, and phase-behavior processes. The well-leakage model used a 2-D radial geometry with the well at the center. The initial conditions in the reservoir were established using capillary-gravity equilibrium for average CO_2 saturations ranging from 0.01 to 0.5 and for a range of reservoir overpressure conditions from 0.03 MPa to 5.2 MPa. The constant pressure, temperature, and saturation boundary conditions at the radial boundary in the storage reservoir were used, assuming that the leakage effect is limited to a local effect in a large plume. The investigation considered 15 different well and reservoir permeability combinations, ranging from 0.01 to 1 darcy in the reservoir and 0.1 to 1,000 darcies in the well.

Coupled effects between the reservoir flow restrictions and well leakage have been found to be relatively weak if well-to-reservoir permeability ratios are 100 or less and if CO_2 saturations in the reservoir are not too small. For higher CO_2 saturations in the reservoir, the maximum effect of coupling on well leakage is less than a factor of three even for well-to-reservoir permeability ratios of 10^5. However, coupled effects on well leakage can be stronger when CO_2 saturation levels in the reservoir are small, such that the CO_2 occupies a relatively thin layer along the top of the reservoir, an effect described here as thin-layer flow behavior. A thick-layer response means H_2O enters the well entirely as a dissolved component in the CO_2. A thin-layer response means that H_2O enters that well as a bulk aqueous phase in addition to H_2O dissolved in the CO_2. For thin-layer cases with large well to reservoir permeability ratios, the leakage rates can vary by nearly two orders of magnitude as a result of coupling with the reservoir. This stronger coupling between well leakage and the reservoir for cases where the CO_2 layer in the reservoir is thin only applies to CO_2 leakage; coupling effects on H_2O leakage rates are not as strong, although the composition of the aqueous phase is significantly affected.

The reservoir CO_2 saturation immediately below the well was found to change in response to well leakage. However, the saturation in the well cannot be entirely explained by either the initial reservoir saturation state or even to the saturation at the base of the well during the leakage. The saturation in the well was found to be correlated with various factors such as well permeability, reservoir overpressure, and reservoir permeability, in addition to saturation in the reservoir. These results suggest that some degree of coupling is needed in the well-leakage process model used to calibrate a well-leakage reduced-order model in order to represent the saturation differences between the reservoir and the well.

Additional calculations suggested that the overlying shale would be important not only for the heat exchange but also for the water exchange during the leakage, especially in the long-term behavior. The presence of semipermeable shale may have two competing effects: (1) increase CO_2 saturation in a leaky well, which could increase CO_2 relative permeability and CO_2 leakage rate, and (2) more rapidly dissipate overpressure, which could reduce the leakage rate.

The calculations were primarily intended to investigate steady-state well leakage. However, the process-model simulations also provided information on transient well leakage. Results show that the primary transient response, in which CO_2 initially moves up the well, can be prolonged for low-permeability wells, with 0.1-darcy wells having transient periods on the order of 1,000 years, 1-darcy wells having transient periods on the order of 100 years, and 10-darcy wells having transient periods on the order of 10 years. These time frames will be sensitive to reservoir

depth and overpressure, among other factors. Well-leakage response always starts at a low level of leakage and increases until steady-state conditions are achieved. Therefore, quasi-steady-state leakage models will, in general, overestimate leakage during the transient period. Depending on the time frame of risk assessment, this overestimate could be substantial if leakage occurs predominantly through lower-permeability wells.

For thin-layer flow behavior, secondary transients can also be induced in the reservoir by the well-leakage flow. These transients differ from primary transients in that the CO_2 leakage peaks and then decreases to some steady-state level. Therefore, a steady-state model will underestimate peak leakage rates. Although typically weak, these transients last for even a longer time than primary transients, with durations on the order of 100,000 years. In the most extreme case, a secondary transient persisted for more than 250,000 years during which the CO_2 leakage rate decreased by about 98 percent from its peak value shortly after CO_2 breakthrough.

PROMs for CO_2 and water-leakage rates through wells were calibrated from results of coupled reservoir-well simulations using non-linear relative permeability functions. Saturations in the well cannot be represented accurately by saturations at the base of the well, as determined by a reservoir simulator. It was necessary to correlate well saturations with well permeability, reservoir overpressure, reservoir permeability, and the initial CO_2 saturation below the well for use in the PROMs. H_2O movement through the well at low rates can be affected by the flow of water dissolved in CO_2. This impacts the aqueous density in the well, because H_2O entering the well dissolved in CO_2 does not transport salts from the storage reservoir. Adequate representation of H_2O leakage flow in the PROM required a correlation between known factors affecting thin-layer/thick-layer flow behavior and the aqueous density in the well. The PROMs give results with mean-square relative errors of 38 percent for CO_2 and 52 percent for H_2O mass flow rates as compared with TOUGH2-ECO2M simulations. One caveat concerning the results here is that a large number of parameter variations have not been investigated, including the effects of different relative permeability parameters, well penetration into the storage reservoir, and well depth.

Several PROMs are potentially useful for estimating well leakage. These PROMs range from more complex numerical-simulation approaches to simple analytical methods. A number of complexities for well leakage have been identified in this report, including multi-phase, multi-component effects, interactions of well leakage with flow processes in the reservoir and exchange with low-permeability shales, plus significant transient flow effects in the well and reservoir. Multi-phase, multi-component effects have been treated through analytical PROMs, using correlations to incorporate the more complex effects of phase saturation and aqueous density in the well. However, additional significant complexities, in particular transient effects and interactions of well leakage with low-permeability shales, still require further PROM development. More complex PROMs appear to be necessary to address these issues; otherwise, substantial conservatism may be required to avoid underestimation of leakage risk.

8. REFERENCES

Audigane, P.; Gaus, I.; Czernichowski-Lauriol, I.; Pruess, K.; Xu, T. Two-dimensional reactive transport modeling of CO_2 injection in a saline aquifer at the Sleipner site. *American Journal of Science* **2007,** *307*, 974–1008.

Bachu, S.; Bennion, D. B. Experimental assessment of brine and/or CO_2 leakage through well cements at reservoir conditions. *Int. J. Greenhouse Gas Control* **2009,** *3*, 494–501.

Bachu, S.; Bennion, D. B. Effects of in-situ conditions on relative permeability characteristics of CO_2-brine systems. *Environ Geol* **2008,** *54*, 1707–1722.

Benson, S.; Cook, P. Underground geologic storage. In *IPCC special report on carbon dioxide capture and storage*; Bert Metz, B., Davidson, O., de Coninck, H., Loos, M., Meyer, L., Eds.; Working Group III of the Intergovernmental Panel on Climate Change; Cambridge University Press, 2005.

BP, 2012, In Salah CO_2 Storage Project, http://www.bp.com/sectiongenericarticle.do?categoryId=9033334&contentId=7061356.

Busrt, J. F. Argillaceous sediment dewatering. *Annual Review of Earth and Planetary Sciences* **1976,** *4*, 293–318.

Carey, J. W.; Wigand, M.; Chipera, S. J.; WoldeGabriel, G.; Pawar, R.; Lichtner, P. C.; Wehner, S. C.; Raines, M. A.; Guthrie, G. D. Analysis and performance of oil well cement with 30 years of CO_2 exposure from the SACROC unit, West Texas, USA. *Int. J. Greenhouse Gas Control* **2007,** *1*, 75–85.

Carey, J. W.; Svec, R.; Grigg, R.; Zhang, J.; Crow, W. Experimental investigation of wellbore integrity and CO_2-brine flow along the casing-cement microannulus. *Int. J. Greenhouse Gas Control* **2010,** *4*, 272–282.

Celia, M. A.; Nordbotten, J. M.; Court, Dobossy, M.; Bachu, S. Field-scale application of a semi-analytical model for estimation of CO_2 and brine leakage along old wells. *International Journal of Greenhouse Gas Control* **2011,** *5*, 257–269.

Cihan, A.; Birkholzer, J. T.; Zhou, Q. Pressure Buildup and Brine Migration During CO_2 Storage in Multilayered Aquifers. *Ground Water* **2012**.

Duguid, A.; Radonjic, M.; Scherer, G. W. Degradation of cement at the reservoir/cement interface from exposure to carbonated brine. *Int. J. Greenhouse Gas Control* **2011,** *5*, 1413–1428.

Ebigbo, A.; Class, H.; Helmig, R. CO_2 leakage through an abandoned well: problem-oriented benchmarks. *Comput. Geosci.* **2007,** *11*, 103–115.

Friedmann, S. J. *Carbon capture and storage*; UCRL-BOOK-235276; 2007.

Jordan, A.; Stauffer, P. Personal communication, 2011.

Nordbotten, J. M.; Kavetski, D.; Celia, M.; Bachu, S. Model for CO_2 leakage including multiple geological layers and multiple leaky wells. *Environ. Sci. Technol.* **2009,** *43*, 743–749.

Pan, L., Oldenberg, C. M., Wu, Y.-S., Pruess, K. *T2Well/ECO2N version 1.0: multiphase and non-isothermal model for coupled wellbore-reservoir flow of carbon dioxide and variable salinity water*; LBNL-4291E; Lawrence Berkeley National Laboratory: Berkeley, CA, 2011.

Pruess, K. *ECO2M: a TOUGH2 fluid property module for mixtures of water, NaCl, and CO_2, including super- and sub-critical conditions, and phase change between liquid and gaseous CO_2*; LBNL-4950E; Lawrence Berkeley National Laboratory: Berkeley, CA, 2011a.

Pruess, K. Modeling CO_2 leakage scenarios, including transitions between super- and sub-critical conditions, and phase change between liquid and gaseous CO_2. *Energy Procedia* **2011b,** *4*, 3754–3761.

Razavi, S.; Tolson, B. A.; Burn, D. H. Review of surrogate modeling in water resources. *Water Resources Research* **2012,** *48*.

Sabirzyanov, A. N.; Il'in, A. P.; Akhunov, A. R.; Gumerov, F. M. Solubility of water in supercritical carbon dioxide. *High Temperature* **2002,** *40*, 203–206.

Schmidt, G. W. Interstitial water composition and geochemisty of deep Gulf Coast shales and sandstones. *The American Association of Petroleum Geologists Bulletin* **1973,** *57*, 321–337.

Watson, T. L.; Bachu, S. Identification of wells with high CO_2-leakage potential in mature oil fields developed for CO_2-enhanced oil recovery. In Paper SPE 11294, SPE Improved Oil Recovery Symposium, Tulsa, Oklahoma, April 19–23, 2008.

Watson, T. L.; Bachu, S. Evaluation of the potential for gas and CO_2 leakage along wellbores. *SPE Drilling & Completion* **2009,** *24*, 115–126.

Zhou, Q.; Birkholzer, J. T.; Tsang, C.-F.; Rutqvist, J. A method for quick assessment of CO_2 storage capacity in closed and semi-closed saline formations. *International Journal of Greenhouse Gas Control* **2008,** 626–639.

APPENDIX – PROM CALIBRATIONS TO AN UNCOUPLED WELL-LEAKAGE PROCESS MODEL

A set of 961 different cases were computed by Jordan and Stauffer (2011) using the LANL uncoupled well-leakage process model. These results are used here to test and calibrate a version of the PROM discussed in Section 5. Pressure, saturation, and temperature are fixed model-boundary conditions at the base of the model. Both the process model and PROM used linear relative permeability functions. In this case, the PROMs have a single adjustable calibration parameter, β, which is a multiplicative factor for the pressure gradient.

$$\dot{m}_g = -\frac{Ak_b k_{rg}}{\nu_g}\left(\beta\frac{dp}{dz} + \rho_g g\right) \tag{A1}$$

$$\dot{m}_w = -\frac{Ak_b k_{rw}}{\nu_w}\left(\beta\frac{dp}{dz} + \rho_w g\right) \tag{A2}$$

The optimum value of β to minimize the root-mean-square relative error between the PROM and the process model for both CO_2 and water is found to be 0.89, shown in Figure A-1.

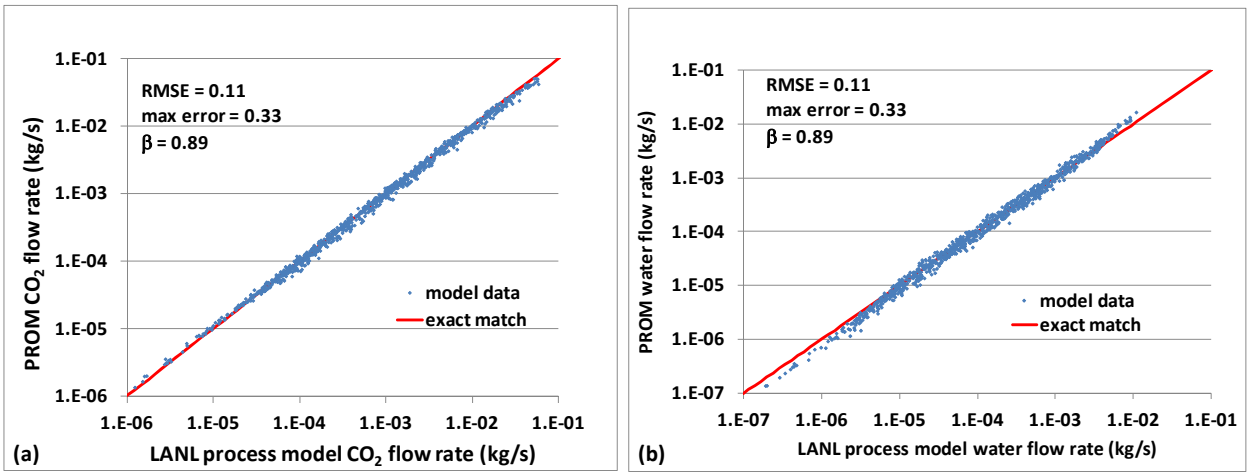

Figure A-1: Calibrated PROMs using uncoupled well-leakage process model results. (a) CO_2 flow rate PROM comparison; (b) Water flow rate PROM comparison. Note that root-mean-square errors (RMSE) shown here are relative errors.

The use of more fitting coefficients can always produce a better fit to data. A PROM with additional parameters was developed to test the ability of the PROM to achieve a 10 percent maximum error target. This higher-order PROM was constructed using the LANL uncoupled well-leakage process model results. Given a target of 10 percent maximum error between the higher-order PROM and associated process model, the fitting coefficient, β, for the well-leakage PROMs in equations (A1) and (A2) was generalized to be a function of known parameters available from the process model runs used to calibrate the PROMs. A single equation was retained to describe the flow of each phase over all parameter conditions; however, to achieve the desired maximum error, β was allowed to vary independently for CO_2 and water PROMs, i.e.,

$$\dot{m}_g = -\frac{Ak_b k_{rg}}{\nu_g}\left(\beta_g \frac{dp}{dz} + \rho_g g\right) \tag{A3}$$

$$\dot{m}_w = -\frac{Ak_b k_{rw}}{\nu_w}\left(\beta_w \frac{dp}{dz} + \rho_w g\right). \tag{A4}$$

The additional parameters used to increase the model fit to the data were derived by trial and error and inspection of the data. The CO_2 fitting coefficient, β_g was found to require five variables to meet the 10 percent maximum error goal:

$\left(S_{CO_2}\right)^2$: square of the CO_2 saturation at the bottom of the well

$D_n\left(\frac{P_b-P_s}{D}\right)_n$: normalized depth times the normalized average pressure gradient

$\ln(P_b - P_s)$: logarithm of the bottom pressure minus the surface pressure

$\left(\frac{P_b-P_s}{D}\right)_n + \left(S_{CO_2}\right)_n + D_n$: sum of normalized pressure gradient, CO_2 saturation (at bottom of well), and normalized well depth

$\left\{\left(\frac{P_b-P_s}{D}\right)_n + \left(S_{CO_2}\right)_n + D_n\right\}^3$: sum of normalized pressure gradient, CO_2 saturation (at bottom of well), and normalized well depth cubed

The term "normalized" means the parameter value (depth or pressure gradient) for a given case minus the minimum value investigated, divided by the total range for that parameter (maximum minus minimum).

The regression equation for the fitting coefficient for CO_2 is,

$$\begin{aligned}\beta_g = c_{g0} + c_{g1}\left(S_{CO_2}\right)^2 + c_{g2}D_n\left(\frac{P_b - P_s}{D}\right)_n + c_{g3}\ln(P_b - P_s) \\ + c_{g4}\left\{\left(\frac{P_b - P_s}{D}\right)_n + \left(S_{CO_2}\right)_n + D_n\right\} \\ + c_{g5}\left\{\left(\frac{P_b - P_s}{D}\right)_n + \left(S_{CO_2}\right)_n + D_n\right\}^3\end{aligned} \tag{A5}$$

The coefficients are:

c_{g0} = -0.14641443897795, c_{g1} = 0.196929174507627, c_{g2} = -0.160595700555032, c_{g3} = 0.0621489973105301, c_{g4} = 0.0126931621921657, c_{g5} = -0.0630047400478965

The greater error in the original PROM for water resulted in a need for additional correlation variables as compared with CO_2 to bring the maximum error below 10 percent. The water fitting coefficient, β_w was found to require 11 variables:

$\left(S_{CO_2}\right)^2$: square of the CO_2 saturation at the bottom of the well

$(P_b - P_s)/T_b$: bottom pressure minus the surface pressure divided by the bottom hole temperature

S_{CO_2}/T_b: CO_2 saturation divided by the temperature at the bottom of the well

$D_n\left(\frac{P_b-P_s}{D}\right)_n$: normalized depth times the normalized average pressure gradient

$\left(S_{CO_2}/T_b\right)^2$: CO_2 saturation divided by the temperature at the bottom of the well squared

$S_{CO_2 n}\left(\frac{P_b-P_s}{D}\right)_n$: normalized saturation times the normalized average pressure gradient

T_b: temperature at the bottom of the well

$\left\{\left(\frac{P_b-P_s}{D}\right)_n + \left(S_{CO_2}\right)_n + D_n\right\}^{-1}$: inverse sum of normalized pressure gradient, CO_2 saturation (at bottom of well), and well depth

$\left\{\left(\frac{P_b-P_s}{D}\right)_n + \left(S_{CO_2}\right)_n + D_n\right\}^{-2}$: inverse sum squared of normalized pressure gradient, CO_2 saturation (at bottom of well), and well depth

$\{\ln(kk_r/\nu)\}^2$: logarithm of the effective water permeability divided by the water kinematic viscosity squared

$\left\{\left(S_{CO_2}\right)_n + D_n\right\}\left\{\left(\frac{P_b-P_s}{D}\right)_n + \left(S_{CO_2}\right)_n + D_n\right\}^{-1}$: sum of normalized CO_2 saturation (at bottom of well), and well depth divided by the sum of normalized pressure gradient, CO_2 saturation (at bottom of well), and normalized well depth

The regression equation for the fitting coefficient for water is,

$$\begin{aligned}\beta_w = {} & c_{w0} + c_{w1}\left(S_{CO_2}\right)^2 + c_{w2}(P_b - P_s)/T_b + c_{w3}S_{CO_2}/T_b + c_{w4}D_n\left(\frac{P_b - P_s}{D}\right)_n \\ & + c_{w5}\left(S_{CO_2}/T_b\right)^2 + c_{w6}S_{CO_2 n}\left(\frac{P_b - P_s}{D}\right)_n + c_{w7}T_b \\ & + c_{w8}\left\{\left(\frac{P_b - P_s}{D}\right)_n + \left(S_{CO_2}\right)_n + D_n\right\}^{-1} \\ & + c_{w9}\left\{\left(\frac{P_b - P_s}{D}\right)_n + \left(S_{CO_2}\right)_n + D_n\right\}^{-2} + c_{w10}\{\ln(kk_r/\nu)\}^2 \\ & + c_{w11}\left\{\left(S_{CO_2}\right)_n + D_n\right\}\left\{\left(\frac{P_b - P_s}{D}\right)_n + \left(S_{CO_2}\right)_n + D_n\right\}^{-1}\end{aligned} \tag{A6}$$

The coefficients are:

c_{w0} = 1.04790825869015, c_{w1} = 0.196929174507627, c_{w2} = -0.411656301288367, c_{w3} = -9.37918173219181, c_{w4} = -0.0322655130414872, c_{w5} = -177.454018926526, c_{w6} = 0.107580946942097, c_{w7} = -0.000612768406188155, c_{w8} = -0.00805293623664742, c_{w9} = 0.000248698154424544, c_{w10} = 0.0000395403275106975, c_{w11} = 0.069406356442926

The results for the regression-calibrated CO_2 and water PROMs are shown in Figure A-2 and their error distributions are shown in Figure A-3.

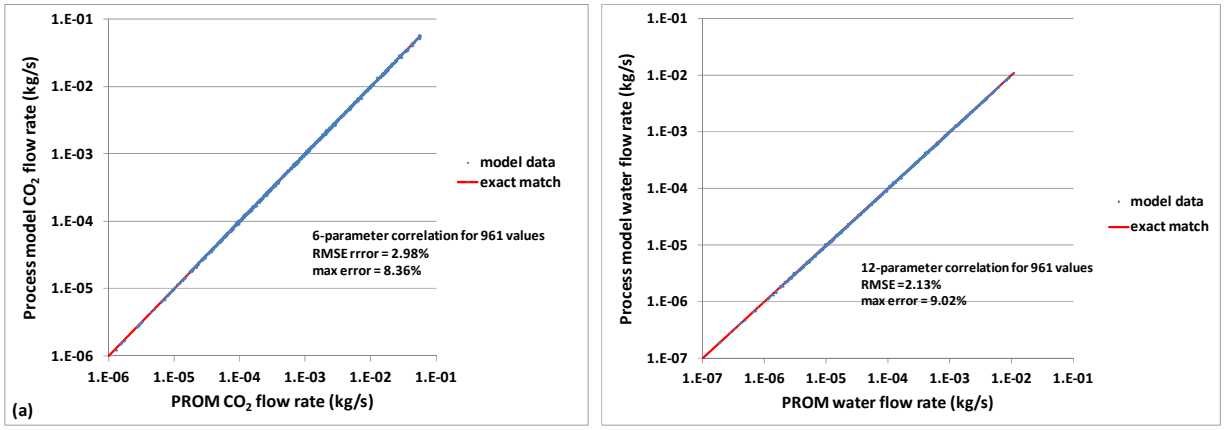

Figure A-2: Calibrated higher-order PROMs using uncoupled well-leakage process model results. (a) CO_2 flow rate PROM comparison; (b) Water flow rate PROM comparison. Note that root-mean-square errors (RMSE) shown here are relative errors.

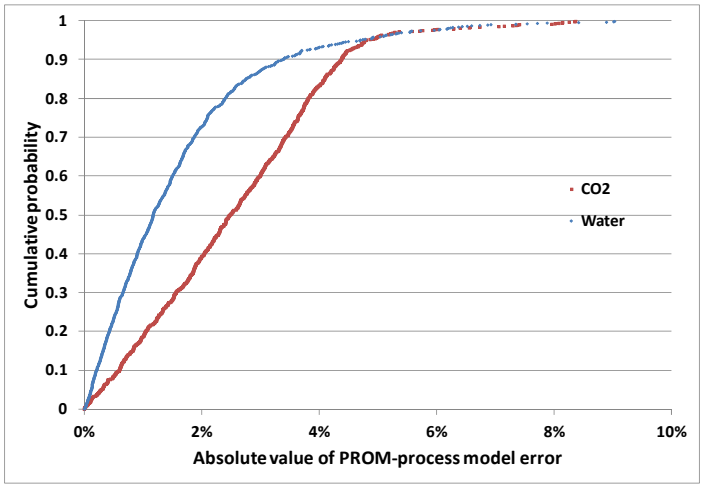

Figure A-3: PROM error distributions for CO_2 and water.

Given that each PROM is regressed against 961 independent process model results, the 6 and 12-parameter regressions for CO_2 and water, respectively, are not likely "overfitting" the data. The maximum regression *p*-value for coefficients from both regressions is about 2×10^{-7} (for c_{g0} in the CO_2 regression). Therefore, all of the correlation parameters are statistically significant.

As can be seen, the 12-parameter water PROM actually keeps errors lower compared to the 6-parameter CO_2 PROM over cumulative probabilities up to about 0.96, but a few "difficult" cases at the tail of the distribution drive the need for additional parameters for the water flow rate.

nrap

National Risk
Assessment Partnership

NRAP is an initiative within DOE's Office of Fossil Energy and is led by the National Energy Technology Laboratory (NETL). It is a multi-national-lab effort that leverages broad technical capabilities across the DOE complex to develop an integrated science base that can be applied to risk assessment for long-term storage of carbon dioxide (CO_2). NRAP involves five DOE national laboratories: NETL-RUA, Lawrence Berkeley National Laboratory (LBNL), Lawrence Livermore National Laboratory (LLNL), Los Alamos National Laboratory (LANL), and Pacific Northwest National Laboratory (PNNL). The NETL-RUA is an applied research collaboration that combines NETL's energy research expertise in the Office of Research and Development (ORD) with the broad capabilities of five nationally recognized, regional universities—Carnegie Mellon University (CMU), The Pennsylvania State University (PSU), the University of Pittsburgh (Pitt), Virginia Tech (VT), and West Virginia University (WVU)—and the engineering and construction expertise of an industry partner (URS Corporation).

NRAP Technical Leadership Team

Jens Birkholzer
LBNL Technical Coordinator
Lawrence Berkeley National Laboratory
Berkeley, CA

Grant Bromhal
NETL Technical Coordinator
Lead, Reservoir Working Group
Office of Research and Development
National Energy Technology Laboratory
Morgantown, WV

Chris Brown
PNNL Technical Coordinator
Lead, Groundwater Working Group
Pacific Northwest National Laboratory
Richmond, WA

Susan Carroll
LLNL Technical Coordinator
Lawrence Livermore National Laboratory
Livermore, CA

Laura Chiaramonte
Lead, Natural Seals Working Group
Lawrence Livermore National Laboratory
Livermore, CA

Tom Daley
Lead, Monitoring Working Group
Lawrence Berkeley National Laboratory
Berkeley, CA

George Guthrie
Technical Director, NRAP
Office of Research and Development
National Energy Technology Laboratory
Pittsburgh, PA

Rajesh Pawar
LANL Technical Coordinator
Lead, Systems Modeling Working Group
Los Alamos National Laboratory
Los Alamos, NM

Tom Richard
Deputy Technical Director, NRAP
The Pennsylvania State University
NETL-Regional University Alliance
State College, PA

Brian Strazisar
Lead, Wellbore Integrity Working Group
Office of Research and Development
National Energy Technology Laboratory
Pittsburgh, PA

nrap
National Risk
Assessment Partnership

Sean Plasynski
Deputy Director
Strategic Center for Coal
National Energy Technology Laboratory
U.S. Department of Energy

Jared Ciferno
Director
Office of Coal and Power R&D
National Energy Technology Laboratory
U.S. Department of Energy

Robert Romanosky
Technology Manager
Office of Coal and Power R&D
National Energy Technology Laboratory
U.S. Department of Energy

Regis Conrad
Director
Division of Cross-cutting Research
Office of Fossil Energy
U.S. Department of Energy

NRAP Executive Committee

Cynthia Powell
Director
Office of Research and Development
National Energy Technology Laboratory
U.S. Department of Energy

Alain Bonneville
Laboratory Fellow
Pacific Northwest National Laboratory

Donald DePaolo
Associate Laboratory Director
Energy and Environmental Sciences
Lawrence Berkeley National Laboratory

Melissa Fox
Chair, NRAP Executive Committee
Program Manager
Applied Energy Programs
Los Alamos National Laboratory

Julio Friedmann
Chief Energy Technologist
Lawrence Livermore National
Laboratory

George Guthrie
Technical Director, NRAP
Office of Research and Development
National Energy Technology Laboratory

NRAP Technical Report Series